Universidad de Concepción

Dirección de Postgrado

Facultad de Ciencias Físicas y Matemáticas - Programa de Magíster en Ciencias con mención en Física

NuSTAR Serendipitous Survey: Results from Magellan (NuSTAR Serendipitous Survey: Resultados de Magallanes)

Tesis para optar al grado de Magíster en Ciencias con mención en Física

Por

CARLA ELIZABETH FUENTES MUÑOZ

Concepción - Chile
2016

Profesor Guía: Dr. Ezequiel Treister
Departamento de Astronomía, Facultad de Ciencias Físicas y Matemáticas
Universidad de Concepción

Resumen

Nuclear Spectroscopic Telescope Array (*NuSTAR*) es el primer observatorio de altas energías (>10 keV) que usa óptica de enfoque. Uno de sus principales objetivos es identificar las fuentes que producen el peak (E $\approx 20-30$ keV) de la radiación de fondo cósmica en rayos-X (CXB, por su sigla en inglés). La búsqueda de Serendipitous de *NuSTAR* es uno de los tres componentes de inspección extragálacticos que encuentra fuentes que están en las regiones del fondo del objetivo de ciencia. *NuSTAR* resuelve directamente $\approx 37\%$ de la emisión del CXB en la banda $8-24$ keV.
Para maximizar el impacto científico de las observaciones en rayos-X e identificar la naturaleza de las fuentes serendipitous de *NuSTAR*, es necesario medir sus redshifts. Con el fin de contribuir a la completitud de identificación espectroscópica, el principal objetivo de ésta tesis es identificar las 35 fuentes detectadas del hemisferio sur. 20 de estas fuentes corresponden al 10% de las fuentes serendipitous con magnitudes $R > 20$, es decir, contribuimos al análisis de la naturaleza del 10% de las fuentes más débiles de las serendipitous.
Para esto, hemos usado tres instrumentos diferentes que proveen una cobertura espectral de $\sim 4000-9000$ Å, suficiente para detectar líneas de emisión/absorción. Estos son MagE y IMACS del telescopio Magellan, y GMOS del telescopio Gemini-South.
Basados en las líneas espectrales, se clasificaron las fuentes en tres clases: el 22.8% de la muestra se les clasificó como Broad-Line AGN (BLAGN) si tienen líneas de emisión anchas, el 62.9% son Narrow-Line AGN (NLAGN) si tienen líneas de emisión de alta ionización más anchas, y el 14.3% son fuentes galácticas si tiene líneas de Balmer en emisión. Además estudiamos las propiedas obtenidas por *NuSTAR*. Para las fuentes extragalácticas se analiza la luminosidad en rayos-X. En particular, las fuentes NLAGN tienen luminosidades más bajas en comparación con las BLAGN. Por otra parte, 7 de las 8 fuentes BLAGN tienen luminosidades tal que se les define como "quasar en rayos-X", ya que las fuentes BL están menos afectadas por el oscurecimiento.
En orden de obtener candidatas de fuentes oscurecidas para Magallan/Gemini-S, hemos obtenido la razón de banda y las hemos comparado con modelos de N_H. Como es esperado, las fuentes NL tienen valores más altos tal que cuatro de éstas son consistentes con ser oscurecidas ($N_H > 5 \times 10^{23}$ cm^{-2}). Se contruyó además el plano f_X/f_{opt} para las fuentes extragalácticas. Se obtuvo que 20 de las fuentes con $R > 20$ mag tiene valores típicos de AGN de $-1 < log(f_X/f_{opt}) < 1$. Sin embargo, dos de éstas fuentes tienen valores $log(f_X/f_{opt}) < -1$. En acuerdo con la definición de hardness ratio, hemos estudiado los valores para NLAGN y BLAGN. Se encontró que hay una diferencia al momento de medir este valor que está relacionado con el redshift (z) y las luminosidades, tal que a bajo z, las fuentes NL tiende a tener valores más altos de hardness ratio.

Finalmente, se concluye que las fuentes identificadas en esta tesis, pertenece al 10% más débil de la población perteneciente al peak del CXB detectadas por *NuSTAR*, 7 son BLAGN con altos valores de luminosidades en rayos-X, 2 NLAGN tienen fuerte emisión en el óptico, solo 4 NLAGN son candidatas para ser oscurecidas, y en general, las 30 fuentes extragalácticas siguen los valores típicos de $-1 < log(f_X/f_{opt}) < 1$ para AGN.

Abstract

The Nuclear Spectroscopic Telescope Array (*NuSTAR*) is the first focusing optics at high-energy (>10 keV) orbiting observatory. One of the main objective of *NuSTAR* is to complete a sensitive extragalatic survey and identify the source populations that produce the peak (E $\approx 20-30$ keV) of the cosmic X-ray background (CXB). *NuSTAR* is directly resolving $\approx 37\%$ of the CXB emission in the $8-24$ keV band.
The *NuSTAR* Serendipitous survey is one of the three components of the extragalactic survey, that was constructed by searching the background regions of *NuSTAR* pointing for background sources not-associated with the original science target. To maximize the scientific impact from these X-ray observations and identify the nature of *NuSTAR* serendipitous sources, we require imaging with higher sensitivity to identify their optical counterparts and spectroscopic redshifts. In order to contribute to the spectroscopic completeness identification, the main goal of this thesis is to spectroscopically identify detectable sources from the Southern hemisphere. We contribute to the analysis of the 10% of the fainter serendipitous sources.
For this, we used three different instruments, MagE, IMACS from the Magellan and GMOS from Gemini-South telescopes. They provide a spectral coverage from $\sim 4000-9000$ Å in a single exposure, sensitive enough to detect emission/absorption lines. We were able to group the sources into three classes based on their spectral features: 22.8% of the sample are classified as Broad-Line AGN (BLAGN) if they have broad emission lines, 62.9% are classified as Narrow-Line AGN (NLAGN) if they have high-ionization emission lines, and 14.3% are Galactic stars if they have Balmer emission lines. We also study the X-ray data obtained from *NuSTAR*. In particular, of the 30 extragalactic sources detected, the NLAGN are less luminous in comparison to the BLAGN. Moreover, 7 out of 8 of these BLAGN are in the threshold that defines "X-ray quasars". This is due to the BL sources being less affected by obscuration.
In order to obtain obscured candidates for the Magellan/Gemini-S we obtain the band ratio of the sources and compared them with the models for N_H. As was expected the NL sources has higher values, and four sources have values consistent with being obscured at $N_H > 5\times10^{23}$ cm^{-2}. We also construct the f_X/f_{opt} plane for the extragalactic sources. We obtain that these 20 $R > 20$ mag sources have typical AGN values of $-1 < log(f_X/f_{opt}) < 1$. However, two of these sources have values $log(f_X/f_{opt}) < -1$. According to the definition of hardness ratio, we studied the difference of the values for NLAGN and BLAGN. The difference is related to the redshift (z) and luminosities, such that at lower z, NL sources tend to have higher hardness ratio values.

Of the 10% of the fainter population that belongs to the peak of the CXB detected by Nustar, 7 BLAGN have higher X-ray luminosities, 2 NLAGNs are possible candidates with higher obscuration, and 4 NLAGNs with negligible amount of obscuration. We noticed 30 extragalactic sources with values of $-1 < log(f_X/f_{opt}) < 1$ for AGN.

Acknowledgements

Tanto que agradecer, tantas personas involucradas en esta etapa de mi vida que termina que espero poder incluir a cada una de ellas. Partir con mi profesor Ezequiel, quien logró demostrarme el significado de ser un científico y por su infinita paciencia. A mis profesores Niel y Rodrigo, por apoyarme en la última fase de esta tesis.

A mis padres y hermanos, mi primer y fundamental pilar en la vida. Por sus consejos tan sabios en cada pequeño y gran problema que me bombardean. Gracias infinitas a mi mami por las pequeñas preocupaciones conmigo y por darme todo lo que necesito para sobrevivir, gracias eternas a mi daddy por las idas a dejar/buscar a cada actividad que tenía y por darme toda su fortaleza, gracias a mi hermano, por sobre todo enseñarme a vivir contigo; y a los tres, por regalonearme cada que vez que podían.

A mi familia, mis tíos, mis tías, primos, primas, los que están en mi cercanía, los que están más repartidos por el mundo y los que me cuidan desde el cielo. Sin ustedes y las juntas a comer mi vida no sería la misma.

A mis amigos y amigas, el otro pilar de mi vida. A Beki y Lili, por pertenecer a mi vida, por aterrizarme cada vez que yo volaba en un mundo ideal, por estar ahí con un aliento/consejo/abrazo/almuerzo/once infaltable en todos estos años de amistad. Vale, por ser tu, y enseñarme lo loca y especial que puede ser la vida, gracias por el apoyo incondicional que me has dado a través de estos años. A Mary y Vale, por todas las noches de estudio y por todo el ánimo y fe que me han brindado, gracias por estar siempre. Gracias por todos los momentos que he vivido con mis compañeritos de la sala/oficina/ropero/comedor/sala de terapia, a Caddy, Cami (Chumbe), Mabri, Aldito, Dania, Ale, Nelvy, Raúl, han sido muchos momentos de estrés, de congresos, de carretes, de espontáneidad, el diario vivir, pero que sin ellos ésta última etapa hubiese sido muy fome y aburrida. A mi parejita de baile, Felipe Matus, por siempre dar el todo en los diversos estilos de bailes aprendidos juntos. A Diego, por todo lo que me enseñó acerca de la vida, que he podido aplicarla en todo esta etapa. Y doy eternas gracias por la conteción y cuidados que Raúl supo brindarme para no decaer ante el intenso estrés.

Mencionar a las personitas que siempre están ahí apoyando y cuidándome sin recibir nada a cambio, tía Jeanette y Marllory, por siempre aparecer con un tecito, remedios o simplemente con alguna sabia palabra acerca de la vida, gracias por darse el tiempo de conocerme tan bien.

Muchas gracias al grupo de outreach, en particular a E.D.A., gracias a estos grupos pude conocerme a mi misma y en especial, gracias por darme la oportunidad de entregarme al servicio de los demás.

Finalmente, gracias a todas las personitas que me han ayudado sigilosamente a que todos estos años sean más fáciles, tía Marce, Soledad, tía Lucy, Don Victor.

Contents

Resumen **ii**

Abstract **iii**

Acknowledgements **iv**

List of Figures **vi**

List of Tables **vii**

1 Introduction **1**
1.1 Active Galactic Nuclei . . . 2
1.2 *NuSTAR* Serendipitous Survey . . . 6
1.3 Goals . . . 8

2 Observations **9**
2.1 Sample Selection . . . 9
2.2 Data Acquisition . . . 9
2.2.1 MagE . . . 10
2.2.2 IMACS . . . 11
2.2.3 GMOS . . . 11
2.3 Data Reduction . . . 12
2.3.1 MagE data . . . 13
2.3.2 IMACS data . . . 14
2.3.3 GMOS data . . . 15
2.3.4 Flux Calibration . . . 15

3 Observed Spectra and Derived Quantities **17**

4 Multiwavelength Data **27**
4.1 X-ray Properties . . . 27
4.2 Ultraviolet to Mid-Infrared Photometry . . . 28

5 Analysis and Results **32**
5.1 Redshifts and Luminosities . . . 32
5.2 Band Ratios . . . 34
5.3 The X-ray-optical flux plane . . . 37

6 Conclusions **43**

Bibliography **46**

List of Figures

1.1 Illustration of the geometric dependency of the unified AGN model adapted from Urry & Padovani (1995). 4
1.2 X-ray background population synthesis for the modified AGN unification model (thick black solid line) from Treister, Urry, & Virani (2009). 5
1.3 X-ray area curves as a function of 8-24 keV flux for the various *NuSTAR* extragalactic survey components from Aird et al. (2015). 7

2.1 MagE spectra of the standard star LTT3864 from this work. 13
2.2 IMACS spectra of PG_1211p143 mask from this work. 14
2.3 GMOS spectra of ESO415_G002 s4 from this work. 15

3.1 *R*-band magnitude versus redshift for sources with spectroscopic identification in this work compared with L16. 20
3.2 MagE spectra of the run 1; own elaboration. 22
3.3 MagE spectra of the run 2; own elaboration. 23
3.4 IMACS spectra of the run 3; own elaboration. 24
3.5 MagE and IMACS spectra of the run 4; own elaboration. 25
3.6 GMOS spectra of the run 5; own elaboration. 26

5.1 Rest-frame 10−40 keV luminosity ($L_{10-40keV}$) versus redshift, for this work 33
5.2 *NuSTAR* band ratio versus redshifts for this work 35
5.3 The *NuSTAR* 8−24 to 3−8 keV band ratio (BR_{Nu}) versus full-band (3−24 keV) count rate for the sources studied in this work. 36
5.4 The hardness ratio (HR) as a function of redshift; own elaboration. 38
5.5 HR vs. total (10−40 keV) X-ray luminosity; own elaboration. 38
5.6 *R*-band optical magnitude versus X-ray flux in hard X-ray (8−24 keV) from this work. 40
5.7 $f_X/f_{\rm opt}$ versus X-ray flux in hard X-ray (8-24keV) from this work. 41
5.8 $f_X/f_{\rm opt}$ versus X-ray flux in full X-ray (3-24keV) from this work. 41
5.9 f_X/f_{opt} versus $L_{10-40\rm keV}$ from this work. 42
5.10 f_X/f_{opt} versus $L_{10-40\rm keV}$ in logarithmic scale for the whole Serendipitous from this work. 42

List of Tables

2.1 Spectroscopic Observations 10

3.1 Spectroscopic Properties 21

4.1 *NuSTAR* sources properties 29
4.2 Ultraviolet-Mid-Infrared Sources Properties 31

Chapter 1

Introduction

In 1962, Giacconi and his team sent an Aerobee rocket (a small unguided suborbital rocket) carrying three Geiger counters operating in the 1.5 to 6 keV range, leading to the first *Evidence for X-rays from sources outside the solar system* (Giacconi et al., 1962). The goal of the experiment was to study X-rays from the Moon, but they accidentally detected X-rays of extra-solar origin.

In particular, they detected a source in the direction of the galactic center (later identified as Scorpius X-1) and a diffuse emission present in every direction, whose origin and nature was impossible to be determined due to the limited resolution of the experiment. That was the first time that the Cosmic X-ray Background (CXB) was observed and identified as diffuse emission. The physical origin of the CXB has been one of the major topics of research for many years.

It is clear today, thanks to telescopes launched in the last years (e.g., HEAO-1, ROSAT), that the CXB is composed by an integrated emission of many faint point-like extra-galactic sources (Lehmann et al., 2001). The CXB spans a broad energy range, roughly from about 0.1 to 500 keV.

In particular, the dominant population of the CXB are the Active Galactic Nuclei (AGNs: Setti & Woltjer, 1989). The AGN is a compact region in the center of a galaxy that has a much higher than normal luminosity over the electromagnetic spectrum, which host a supermassive black hole (SMBH) in their center (Hasinger, Miyaji, & Schmidt, 2005). Other contributors are galaxies, galaxy clusters, large-scale structures and diffuse hot gas in the Milky Way (Fabian & Barcons, 1992). Resolving the CXB into discrete sources is crucial in understanding the accretion history and evolution of AGNs. Moreover, it will help us to understand how SMBHs will grow relative to their host galaxy over cosmic time (e.g., Croton et al., 2006).

Deep surveys act as particulary effective "time machines" because fainter objects of a given type generally lie at greater distances, and therefore, their emission come from earlier epochs (Brandt & Hasinger, 2005). Thus, sensitivity and resolving power of modern telescopes allow us to see distant regions of our universe revealing a more fascinating and intriguing universe than we could ever expect. Furthermore, using space-borne telescopes will extend the waveband accessible to us giving information on sources unknown until now.

One of the most important findings in the X-rays are made by *Chandra* and *XMM-Newton*, both launched in 1999. The superior sensitivity of these telescopes have the potential to resolve $\approx 90\%$ of the CXB at energies between $0.5-8$ keV (Hasinger et al., 2001; Giacconi et al., 2002). Multiwavelength identification studies indicate that most of the X-ray sources found in the Deep Extragalactic *Chandra* and *XMM-Newton* surveys are AGN (e.g., Hickox & Markevitch, 2006). It is important to highlight, these sensitive X-ray surveys have been limited to photon energies of < 10 keV, and are therefore biased against the identification of heavily obscured AGNs (for which the line-of-sight column density exceeds $N_H \sim$ a few times 10^{23} cm^{-2}). These energy range is low compared to the peak at $\approx 20 - 30$ keV of the CXB, i.e., the extrapolations from lower energies are necessary to characterize the AGN population responsible for the CXB peak.

High energy (>10 keV) X-ray surveys with non-focusing X-ray observatories such as *Swift*-BAT and *INTEGRAL*, have directly resolved $\approx 1 - 2\%$ of the CXB peak into individual AGNs (Krivonos et al., 2007; Ajello et al., 2008). These surveys have been successful in characterizing the local high-energy emitting AGN population (e.g., Tueller et al., 2008) but, being largely confined to $z \lesssim 0.1$, there is limited range for evolutionary studies.

Population synthesis models have succesfully shown, in the context of the AGN unified theory (Antonucci, 1993), that those ones with various level of obscuration and at different redshifts can account for $80\% - 100\%$ of the CXB up to $\sim$100 keV (e.g., Treister & Urry, 2005).

1.1 Active Galactic Nuclei

According with Woltjer (1990), "AGN constitute a somewhat vaguely defined class of objects. It is very well possible that most galaxies have nuclei and that these are active in the sense that there is an energy source in addition to the thermonuclear sources inside the constituent stars. Something is called an AGN if this activity is substantial

in some characteristic, but the quantitative meaning of this is unclear and tied up with experimental or observational possibilities."

AGNs also include those galaxies with high excitation nuclear emission lines called "Seyfert galaxie". The study of AGNs has increased, leading to a better understanding of their physics and properties. Since the first experiment of Giacconi et al. (1962), X-ray astronomy has unraveled a new frontier in the field of AGN research.

AGNs are the brightest object in the Universe (some cases are 10^4 times the luminosity of a typical galaxy). This radiation covers an extraordinarily broad range of wavelengths. Their power comes from the accretion of matter as an accretion disk, that surround the SMBH located at the very center of a galaxy, impulsed by a strong relativistic gravity field.

AGNs can be found in many forms: they span over a wide range of luminosity and present different spectral features, so their classification may be interesting. Hereby, the X-ray band is the most efficient way to detect and finding AGN. This emission is observed in almost all AGN, because X-rays at energies E $>$ 10 keV are not absorbed by the surrounding material unless it is optically thick to Compton scattering. X-rays allows us to study the region close to the SMBH where the most energetic phenomena originate. Deep X-ray surveys can find $z > 4$ AGN that are $\approx 10 - 30$ times less luminous than the ones found in wide-field optical surveys (Brandt & Hasinger, 2005). Such moderate-luminosity AGN are much more numerous and thus more representative of the AGN population than the rare, highly luminous ones.

AGN unification model (Antonucci, 1993) is based on galaxies hosting a SMBH (10^{6-10} $M_\odot$) which actively accretes matter from the surrounding disk, radiating from the radio to X-ray energies.The schematic view of the structure of the AGN, according to our current understanding of the AGN phenomenon and established from observational studies in different spectral bands and modelling (Antonucci, 1993; Urry & Padovani, 1995), is shown in Figure 1.1. The nucleus is surrounded, at a distance of a few gravitational radii (R_S) from the BH, by an accretion disk of hot (T $\sim 10^9$ K) relativistic electrons, this one has a high radiation that emits it at hard X-rays energies, (E $>$ 2 keV). The dense molecular cloud that surrounds the black hole and accretion disk, which is usually supposed to form at parsec-scale is called the torus (orange region). The torus is optically thick and re-radiate the dust and gas from the central regions in infrared and optical regimes. Is also responsible for blocking the emission coming from the central region and, at some level, for the reprocessed emission observed at different wavelengths (Urry & Padovani, 1995).

Thus, if the torus is seen face-on, the view of the central regions is unobscured and the observer sees the Broad Line region (BLR) detecting the broad emissions lines, called type 1 Seyfert. In case the observer's line-of-sight is closer to edge-on, the central regions and thus, the BLR are not seen directly and the Narrow Line region (NLR) is detected, called type 2 Seyfert. Another remarkable morphology of an AGN that was discovered in 1918 (Curtis, 1918) were a pair of relativistic jets. These are plasma structures that are energetic and highly collimated and are launched from the accretion disc. Although not for all the sources we are able to detect them, they propagate to kiloparsecs or more in distance.

The central BH-accretion disk system is surrounded by gas and dust with different densities and ionization states. For example, the **BLR** has an electron density of at least 10^8 cm^{-3}, a gas velocity of $3-10 \times 10^3$ km/s and extends form 0.05 pc to 1 pc. Such systems are usually known as Quasars. The strongest observed lines in them are the Hydrogen Balmer-series (H_α λ6562 Å, H_β λ4861 Å, H_γ λ4340 Å), Lyα λ1216 Å, and prominent lines of abundant ions (MgII λ2798 Å, CIII] λ1909 Å and CIV] λ1549 Å). The other region is the **NLR** with a density of 10^{3-6} cm^{-3}, a gas velocity of $300-1000$ km/s, and they have been resolved in optical at ∼100-300 pc. The electron density in the NLR is low enough that many forbidden transitions are not collitionally suppressed. The [OIII]/H_β flux ratio is usually >3 and the full width half maximum for narrow emission falls in the range $200-900$ km/s.

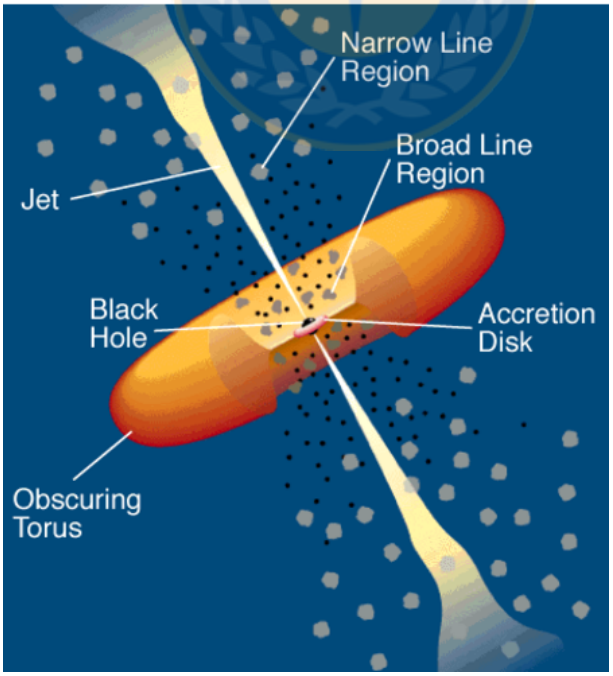

FIGURE 1.1: Illustration of the geometric dependency of the unified AGN model adapted from Urry & Padovani (1995).

Population synthesis models based on studies of the X-ray luminosity and N_H function at lower energies, proposed a model in which obscured and unobscured AGN are combined to explain the X-ray background spectrum. Setti & Woltjer (1989) work postulated that a larger number of obscured AGN relative to unobscured is required to make the resulting spectrum harder. Later works (e.g., Gilli, 2004) clearly shows that optically bright AGNs are not responsible for the bulk of the X-ray background. Using the results of a combination of several surveys in hard X-rays in which both obscured and unobscured AGN are well represented, Ueda et al. (2003) presented an AGN luminosity function that incorporated a luminosity-dependent density evolution, in the sense that low luminosity sources peak at lower redshift, while high luminosity ones peak at a higher redshift and evolve more strongly. Additionally, a dependence of the ratio of obscured to unobscured AGN with luminosity was observed. Thus, Treister, Urry, & Virani (2009) (Figure 1.2) attribute $\gtrsim$ 70% of the emission at this peak to obscured AGNs ($N_H \gtrsim 10^{22}$ cm^{-2}), although the required fraction of Compton-thick ($N_H \gtrsim 10^{24}$ cm^{-2}) AGNs is still uncertain (e.g. Ballantyne et al., 2011). Figure 1.2 show the observed spectrum of the extragalactic CXB from *HEAO 1* (Gruber et al., 1999), *Chandra* (Hickox & Markevitch, 2006), *XMM* (De Luca & Molendi, 2004), *INTEGRAL* (Churazov et al., 2007), and *Swift* (Ajello et al., 2008) data. The dashed gray line shows the CXB spectrum from the AGN population synthesis model of Treister & Urry (2005), The red, blue, and black thin lines show the contribution to this model from unobscured, obscured Compton-thin and Compton Thick AGNs, respectively.

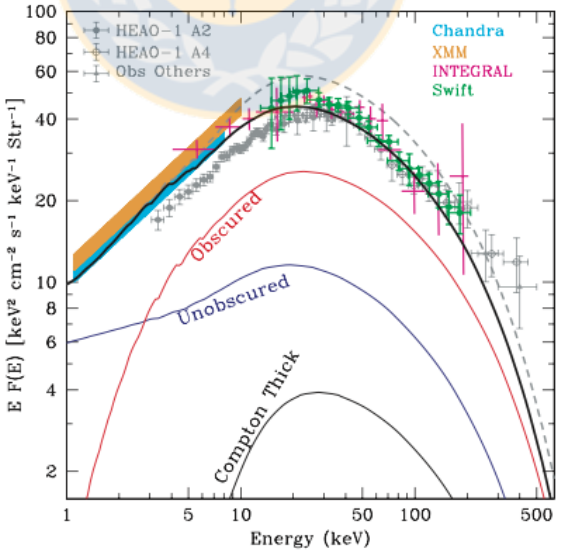

FIGURE 1.2: X-ray background population synthesis for the modified AGN unification model (thick black solid line) from Treister, Urry, & Virani (2009).

1.2 *NuSTAR* Serendipitous Survey

A breakthrough in directly resolving the peak of the CXB has come from the Nuclear Spectroscopic Telescope Array (*NuSTAR*) observatory, which was successfully launched on 2012. *NuSTAR* is the first high-energy (>10 keV) orbiting observatory with focusing optics and has a usable energy range of 3−79 keV (Harrison et al., 2013). Provides ⩾2 orders of magnitude improvement in sensitivity and ∼ 1 order of magnitude in angular resolution over previous E>10 keV observatories, with a flux limit of 2×10^{-14} erg s^{-1} cm−2. The full width at half-maximum of the point-spread function is ∼ 18" and the half-power diameter is ∼ 58".

The *NuSTAR* observatory is comprised of two independent telescopes (A and B), these are two focal plane identical in design modules. The modules have fields-of-view (FoVs) of $\sim 12' \times 12'$, which overlap in sky coverage. The main energy band that *NuSTAR* is focuses on is in the unique $3 - 24$ keV band, which is divided into full ($3 - 24$ keV), soft ($3 - 8$ keV) and hard ($8 - 24$ keV) bands. This full energy band is the most useful band for the relatively faint sources detected in the *NuSTAR* extragalactic surveys, since the combination of instrumental background and a decrease in effective area with increasing energy means that source photons are unlikely to be detected at higher energies, except for the brightest sources.

One of the main goals of *NuSTAR* is to complete a sensitive extragalatic survey and identify the source populations that produce the peak of the CXB at energies between 20−30 keV. The *NuSTAR* Serendipitous survey is one of the three components of the extragalactic survey (Harrison et al., 2013). *NuSTAR* extragalactic survey includes:
(1) NuSTAR-detected sources in the fields of *NuSTAR* targets, similar in principle to the serendipitous surveys undertaken in the fields of *Chandra* and *XMM-Newton* sources;
(2) the major component of the *NuSTAR* Serendipitous survey are $\approx 15 - 20$ ks observations of ≈100 *Swift*-BAT identified AGNs; which covers $\approx 2 - 3$ deg^2 of area to search for Serendipitous sources.
(3) another component are the *NuSTAR* observations of targets not in the ECDF-S, COSMOS, and Galactic-plane surveys are used to search for serendipitous *NuSTAR* sources. The expected coverage of the *NuSTAR* Serendipitous survey in the first two years is ≈3−4 deg^2. Figure 1.3 show the Serendipitous survey (purple doted line), compared to the other components of the *NuSTAR* extragalactic surveys program: *NuSTAR*-COSMOS (blue dashed line; Civano et al., 2015), *NuSTAR*-ECDFS (orange line; Mullaney et al., 2015), and *NuSTAR*-EGS (green dash-dotted line; Aird et al., in prep.). The total area for these blank-field surveys is shown as a long-dashed black line. In this figure, clearly is shown that the Serendipitous survey covers the largest overall area.

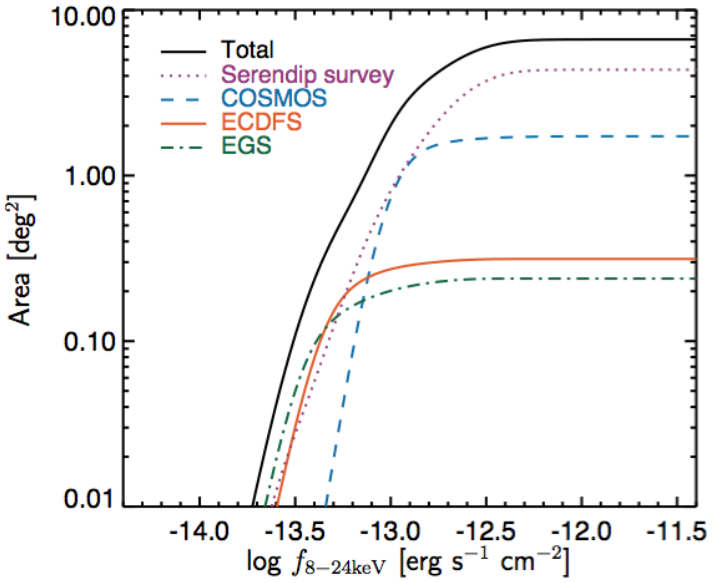

FIGURE 1.3: X-ray area curves as a function of 8-24 keV flux for the various *NuSTAR* extragalactic survey components from Aird et al. (2015).

The survey reach the background regions of almost every non-survey *NuSTAR* pointing for background sources unassociated with the original science target. The Serendipitous survey not only covers the largest overall area but also covers an area comparable to the dedicated deep surveys at fainter fluxes. An initial look at 10 Serendipitous survey sources was presented in Alexander et al. (2013). Serendipitous surveys represent an efficient and economical way to sample wide sky areas, and provide substantial data sets with which to examine the X-ray emitting population and search for extreme populations.

Harrison et al. (2016) present source number counts at $3-8$ keV and $8-24$ keV energies from the full survey program and show that *NuSTAR* is directly resolving $33\%-39\%$ of the CXB emission in the $8-24$ keV band, which is a significant advancement compared to the $1\%-2\%$ resolved to-date, a factor $\sim 15-30$ times more than previous high-energy X-ray observatories. To determine the overall sky coverage of the survey as a function of flux sensitivity, Lansbury et al. (2016) (hereafter referred as L16) sum the sensitivity curves for the 331 individual fields. For this work 26 fields were used with an exposure time range for a single FPM (i.e., averaged over FPMA and FPMB) from 16.4 to 320.9 ks.

1.3 Goals

To maximize the scientific impact from these X-ray observations and identify the nature of *NuSTAR* Serendipitous sources, we require accurate imaging to identify their optical counterparts and spectroscopic redshifts. The combination of X-ray and optical data of AGN allows us to study their mutual connection and its evolution over cosmic time.

In order to contribute to the spectroscopic identification, 43 sources from the Southern hemisphere are observed in this thesis. We spectroscopically identified 35 sources, i.e. the 13% (35/276) of the overall sample, and the remaining sources were too faint to be identified.

The magnitude of 20 sources of this subsample is $R >$20. Considering completeness for the southern hemisphere, the sources in this thesis are also $\approx 56\%$ of the fainter sources ($R >$20 mag) in the southern hemisphere.

In order to understand the composition of the CXB at $\sim 20-30$ keV and the obscuration of the high-energy emitting AGN population, a detailed characterization is presented for these sources using band ratio and hardness ratio definition, and the X-ray-to-optical flux ratio sources.

Chapter 2

Observations

2.1 Sample Selection

As of November 2015 the *NuSTAR* Serendipitous catalog has 497 sources (L16). Only 57 ($\approx 11\%$) had pre-existing spectroscopic coverage, primarily from the SDSS. For that reason, the *NuSTAR* Serendipitous survey has undertaken a campaign of dedicated spectroscopic follow-up in the optical-IR bands (See Section 3.3.1 of L16), observing 276 targets of which 141 now have redshifts. The southern serendipitous sources have not been extensively observed since most previous observation were made with Palomar and Keck telescopes.

We selected a sample of southern sources from the December 2013 to January 2016 versions of the *NuSTAR* Serendipitous catalog which do not have previous spectroscopic observations. The selection cutoff was R magnitude brighter than 14 mag and Declination $< 20^{\circ}$ and a high Galactic latitude ($|b| > 10$), to ensure that our sample is dominanted by extragalactic sources (and not contaminated with the Galactic plane). Sub-samples of this sample, depending on the visibility during the semester, were proposed to Magellan I, Magellan II and Gemini-S for 2013 to 2016. Over the five observing campaigns reported here, a total of 43 sources were observed.

2.2 Data Acquisition

The data were taken with the MagE/Magellan I (6.5 m, Baade) telescope in program ID's CN2013B-86, CN2014B-113; IMACS/Magellan II (6.5 m, Clay) telescope in program ID CN2015A-87; MagE and IMACS/Magellan II in program ID CN2016A-93; and GMOS/Gemini-South observatory (8.1 m) in program ID GS-2016A-Q-45. Table 2.1 list

the observational parameters for the different instruments used in the thesis, including the observing run starting date (UT), telescope, instrument, total number of observed sources, and the total exposure time, for each night.

The observing conditions were met and therefore they had no adverse effect on the quality of the data. Thus, the sky conditions on all nights were photometric, allowing us to use observations of photometric standard stars to calibrate all data.

TABLE 2.1: Spectroscopic Observations

Run ID[a]	UT start Date[b]	Telescope[c]	Instrument[d]	Sources[e]	T_{exp}(s)[f]
1	2013.December.05	Magellan	MagE	10	9900
2	2014.September.24	Magellan	MagE	11	10800
3	2015.March.18	Magellan	IMACS	10	11400
4	2016.February.08	Magellan	MagE & IMACS	10	11700
5	2016.February.02	Gemini-S	GMOS	7	3750

Notes.
[a]ID assigned to each observing run. date. [b] Observing run start date. [c] and [d] The telescope and instrument used. [e] The number of sources observed per run. [f] Total exposure time per night. This table was elaborated using data from this work.

2.2.1 MagE

During the runs 1 and 2 of our experiment the Magellan Echellette (MagE) echelle was located on the Magellan II (Clay), but was later (run 4) transferred to the Magellan I (Baade) telescope at Las Campanas Observatory, Chile. MagE is a single object optical echelle spectrograph providing spectral coverage from $3200-10000$Å in a single exposure, with a moderate resolution ($R \approx 1000-8000$), achieving R= 4100 (22 km/s pixel) with a 1" slit (Marshall et al., 2008).

The detector is a 2048 $\times$ 1024 pixel CCD with 13.5μ pixels, placed at the prime focus of a vacuum Schmidt camera. The instrument itself is easy to operate, but presents challenges in the data reduction. To overcome the difficulties of flat-fielding over a very large wavelength range, a combination of focused and de-focused Xenon (Xe) lamps were utilised to provide enough flux in the near ultraviolet, and quartz lamps were used for the red end of the spectrum. Another remarkable challenge is the curving of the orders on the detector, as can be seen in Figure 2.1. This means that the spectral features are also tilted, with a different inclination along each order. This makes the sky subtraction particularly difficult, since when the order is flattened the sky line may not be perpendicular to the continuum, and hence could not be removed from the final spectra. We will discuss in more detail the data reduction of MagE spectra in the following section.

The observations on MagE were made during 3 nights: the first one on UT 2013 December 7, the second one on UT 2014 September 27 and the third on UT 2015 March 18, in which the slit 1.5", 1.0" and 1.0", respectively, were used for each night. The slits are 10" long with a plate scale of 0.3" per pixel on the detector. Here different exposure times were selected in order to detect optical counterparts with a limited magnitude of ≈22 and to obtain emission/absorption lines. Exposure times varied between 600 and 1200 seconds, depending on the target apparent magnitude, with a total integration time of 27 ksec, see Table 2.1 for more details.

2.2.2 IMACS

Inamori Magellan Areal Camera and Spectrograph (IMACS, Bigelow et al., 1998) is mounted on the Baade Magellan 65 m telescope at Las Campanas Observatory. The field of view of the IMACS camera is 22'30" × 21'10". It uses a low resolution grism (usually 200 mm), the GG455 blocking filter, and a 300 lines/mm grating which was sufficient to detect emission and/or absorption lines. A longslit and a multi-slit masks with 1" and 1"5, respectively, were used for this work in order to obtain more than 1 spectra simultaneously. We ensured that if there is a field with at least 4 serendipitous not identified before we make the masks using the software package *MASKGEN*, written and maintained by Ken Clardy (http://www.lco.cl) . In Figure 2.2 we show an example 2D spectrum from the mask. Eight spectra were obtained on the first IMACS run (2015 March 28) and six spectra on run 4 (2016 February 08) with total integration times of 3.17 hr and 1.5 hr, respectively.

2.2.3 GMOS

The Gemini Observatory consists of two 8.1-m diameter, altitude-azimuth mounted telescopes, the Frederick C. Gillett Gemini North telescope on the summit of Mauna Kea on the island of Hawaii, and the Gemini South telescope on the summit of Cerro Pachon in Chile. The Gemini MultiObject Spectrograph (GMOS, Davies et al., 1997) with long slit spectroscopy is mounted on both Gemini telescopes, but we use the south one. The data was successfully taken between January and April 2016. Table 2.1 has more details about the observations. GMOS provide 0.36-0.94 μm long-slit spectroscopy and imaging over a 5.5 square arcminute field of view. The spectrometer contains three separate CCD chips with a gap between each chip of ∼2.8 arcsec (39 pixels) and an overscan region of 32 pixels, as shown in Figure 2.3. Thus, the gaps between the detectors cause small

voids in the wavelength interval covered by a single observation, as seen in Figure 2.3. On the new Hamamatsu CCDs at GMOS-S the two gaps are 4.88 arcsec wide (61 pixels in unbinned mode). The equivalent gap in the wavelength coverage depends on the grating used for the observation.
The science data for this project consists of 6 images taken with a 1 arsec long slit using the R400_G5325 grating, which disperses the light at 0.074nm/pixel. The spectral resolution for GMOS is $R = 1918$ for 0.5 arcsec slit. All of the data files were reduced such that all atmospheric and instrument effects were removed. This reduction process produces the final, clean version of the data that we used in our interpretation.

2.3 Data Reduction

Here we discuss the basic reduction steps applicable to general spectrographs, that include bias subtraction, trimming, overscan correction, flat field correction, and wavelength calibration.

A CCD is a light-sensitive integrated circuit that stores and displays the data for an image in such a way that each pixel in the image is converted into an electrical charge. Given their high quantum efficiencies, linearity of their outputs and ease of use compared to photographic plates, CCDs are used in astronomy for nearly all applications. The data from a CCD requires the following set of calibrations to convert the 2-D images into 1-D spectra:
Bias Correction: The read out noise is an intrinsic property of the device used. To avoid any negative value pixels after the read out, a bias level of hundreds of electrons is added to each pixel. To subtract this level, it is necessary to take zero exposure time frames with the shutter closed to have only the read out noise left, we call these frames as bias frames. To avoid any bias structure, these frames are averaged and subtracted from each science target.
Flat field Correction: As the pixels of a CCD are not equally sensitive there are (small) variations in their response to the incident photons. This needs to be corrected by using the so-called flat field exposures. These are uniform exposures of a featureless continuum. Exposures of the sky during twilight and/or of a tungsten lamp built into the spectrograph are used as flat fields - for this process we employ a lamp in this work. A series of exposures are averaged to find a master flat. In spectroscopy, the flat fields are not "flat" as the spectral shape of any flat field source depends on the wavelength. The master flat is then created by fitting the flat field shape along the wavelength axis with a lower order polynomial and dividing it's average by this fit. The result is a normalised

2-D image with variations of up to a few percent.

Wavelength Calibration: An arc spectrum is used to convert the x-axis from a pixel scale to a wavelength scale. Arcs are usually exposures of lamps of thorium and argon (ThAr), or another combination of gases rich in lines to apply wavelength calibration over the entire range. These are taken with the same setup as the science frames, that are then extracted in the same way as the target spectra. The pixel position of each identified arc line is then compared to its known reference wavelength, and a polynomial is fitted to determine the conversion between the pixels and wavelength. This transformation is then applied to the target spectra.

Spectrum extraction: The final step in processing the spectra is to extract them. This essentially refers to the process of correcting for the night sky background and reducing the spectrum to one dimension. Each pixel in this final 1D spectrum is then the total flux of the object (this is an instrumental flux) corrected for any sky emission.

2.3.1 MagE data

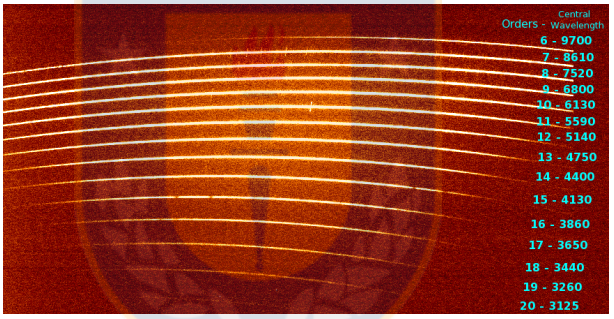

FIGURE 2.1: MagE spectra of the standard star LTT3864 from this work.

There are some differences between echelle data and standard long-slit spectra which make the two data reduction processes different. The main distinctive features of an echelle spectra are two: the object spectrum is arranged in a certain number of orders and each order is curved (Figure 2.1). For these reasons, automatic data reduction pipelines are often developed and they are able to extract and calibrate the spectra in the best possible way. In Figure 2.1 we show the numbered orders from 6 to 20 from top to bottom of the image, respectively, while the wavelength increases from bottom to top. MagE's spectra were reduced using Dan Kelson's MagE pipeline (Kelson, 2003) and IRAFs tasks.

This pipeline generates a data file that contains the information from all the fits files. One important consideration in the reduction with this pipeline is that it is necessary to specify the types of flat (dome and blue) in this data file. After the pipeline make

the wavelength calibration gives us the RMS for each order. The averaged RMS of the wavelength solution fit across all the orders is 0.34 Å.

MagE spectrograph requires some extra calibration data to run the pipeline, as well as three kinds of flat field frames: Xe-Flash frames to locate the order edges, de-focused Xe-Flash frames, for flat fielding the blue end of the spectrum, and Dome flats to construct the flat field at the red end of the spectrum.

MagE's pipeline subtracts the Sky Background and extracts the 1D spectrum, but it was not precise enough to measure the continuum so we decide to do it manually. So as a last step, we extracted the 1D spectra using IRAF's task: *APALL*.

2.3.2 IMACS data

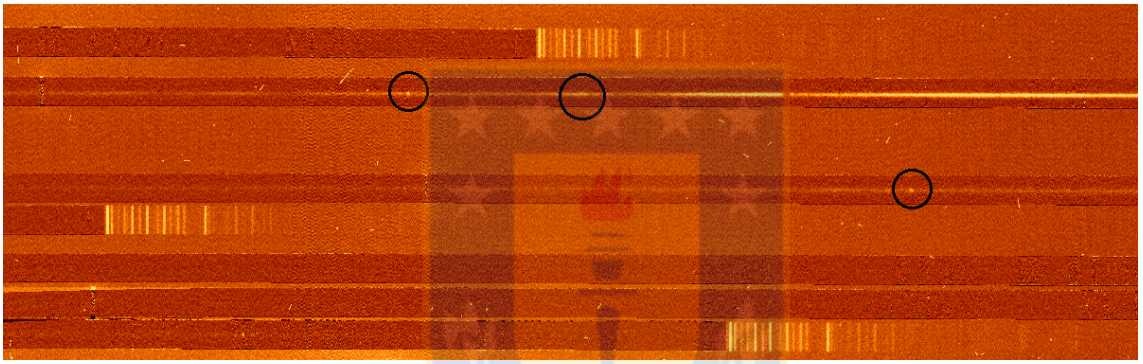

FIGURE 2.2: IMACS spectra of PG_1211p143 mask from this work.

As stated earlier, IMACS data were obtained through longslit and masks. An example of how the masks are viewed after the sky-subtracted is shown in Figure 2.2. Also shows black circles that indicate a emission line. The IMACS' spectra were reduced by the publicly available package Carnegie Observatories System for MultiObject Spectroscopy (**COSMOS** v2.16, written by A. Oemler) to extract and sky-subtract individual 2D linear spectra.

It is necessary to take special care in the reduction of the data, in order to have an accurate wavelength calibration. For this reason, we have to correctly map and align the mask along the slits, and thus, all the calibrations accurately fit to each slit. We align the mask using an iterative routine, taking into account the obtain value of RMS average of 0.24 Å. Even so, the typical residual is about a pixel, and is dominated by systematic errors. These are due to imperfectly-mapped distortions in the IMACS optics. These small errors are removed when we construct and adjust the spectral map. Finally, we subtract the sky using the routine `subsky`.

2.3.3 GMOS data

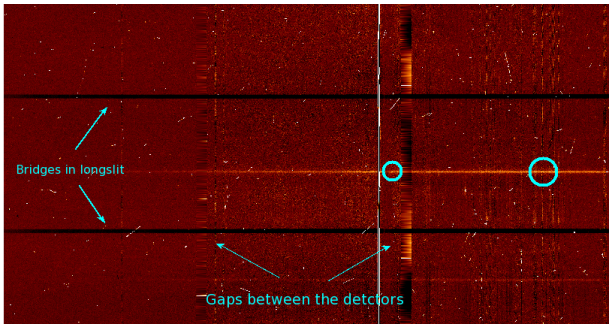

FIGURE 2.3: GMOS spectra of ESO415_G002 s4 from this work.

The GMOS spectra were reduced using Image Reduction and Analysis Facility (IRAF) in particular the GEMINI V13.10 package and GMOS tasks.

The preprocessed master bias file was created from many biases that are not overscan corrected but are trimmed, and finally averaged together. These images are taken with the GMOS shutter closed. In order to create the normalized flat field, it was necessary to obtain the response of the flat source that will adjust the detector by detector instead of slit by slit. And thus, the response function with a single continuum fit made to the average of the rows within each detector and all the rows are normalized, retaining any spatial structure. Our wavelength calibration of GMOS spectra was based on CuAr spectra. We performed the wavelength solution for the arc using the interactive mode with an obtained value of RMS$<$ 0.5 Å. An important parameter in determining the outcome of the wavelength calibration is the order of the function used to determine the wavelength calibration. We decide to use the default value given by `IRAF`, order = 4, because a higher order function could fit undesirable features causing a bad wavelength calibration. Finally, GMOS has a special routine to extract the spectra. Figure 2.3 show the final GMOS longslit reduction of one of the sources. Also show a cyan circles that indicate an emission line.

2.3.4 Flux Calibration

Flux calibration is the procedure to convert from count to physical units an observed spectrum, and thus, calibrates the absolute response of the instrument. We use set of series of steps in order to accurately determine the sensitivity function for the particular spectrograph's facility and observational conditions, following the Equation 2.1. This is applied to compute the observed continuum flux, and thus remove instrumental-response's wavelength-dependency. The sensitivity function is determined by observing

the so-called flux standard objects, usually bright stars. Flux standard stars are observed under ideal conditions of spectrographs for which the sensitivity functions are well calibrated. Public lists of these stars and their spectral flux densities are often made available by the observatory.
Flux calibration require photometric conditions, i.e., no added atmospheric optical depth due to clouds, dust, etc., under excellent seeing conditions.

The steps that we follow for the flux calibration are:

1. Observing the flux standards stars at similar airmass to the main targets.
2. Reducing the standard stars and the program objects in an identical manner.
3. Taking the ratio of observed counts to the published observed flux of the standard stars, and computing the sensitivity function.
4. Applying Equation 2.1 to the serendipitous objects.

The simplest way to follow these calibration steps is that at the end of the raw data reduction for each of the spectrographs, the spectra from MagE, IMACS and GMOS were converted into ASCII format to be read into a PYTHON routine. We obtain the final fluxes using the following equation,

$$I_\lambda = S_\lambda F^o_\lambda \tag{2.1}$$

where I_λ is the measured continuum counts, S_λ is the sensitivity function [counts Åcm^2 sec erg^{-1}], and F^o_λ is the observed continuum flux.

We did not estimate the errors in the flux calibration, this is because it is not much useful for the estimation of redshifts.

Chapter 3

Observed Spectra and Derived Quantities

Optical identifications and redshifts measurements, obtained through spectroscopy, are a prerequisite to the analysis of intrinsic source properties such as luminosity and the amount of obscuration (L16).

Of the 43 sources observed by us 4 were not detected in the continuum or emission lines. These are all at $R > 22$ mag and are excluded from the analysis.

The spectra of the remaining 39 sources are shown in Figure 3.2-3.6. These detected sources have magnitudes in the range from $16 \lesssim R \lesssim 22$ mag. It is noted that there are some features that are common to all our source spectra, hence they are not characteristic of the objects, but have different origins. A first problem is the strong absorption line at $\lambda \approx 7600$ Å, is a feature produced by the atmosphere. And the second issue, in some cases, is the significant spectral noise at $\lambda \geqslant 8500$ Å that is due to a contamination of sky lines, which is difficult to correct properly in the sky-subtraction process.

The typical observed-frame wavelength range covered, for the instrument setups, is $\lambda \sim 3500 - 9000$ Å. At lower redshifts, e.g. z < 0.8, this results in coverage of the following emission lines common to AGNs: [OII] λ3728 Å, H_δ λ4102 Å, H_γ λ4340 Å, H_β λ4861 Å, [OIII] λ5007 Å/λ4959 Å, [OI] λ6300 Å/λ6364 Å, [NII] λ6548 Å/λ6584 Å, $H_\alpha\lambda$6563 Å, and [SII] λ6716 Å/λ673 Å. At higher redshifts, for example z > 0.8, the lines covered are: HeII λ1640 Å, CIII] λ1909 Å, MgII λ2800 Å, CIV λ1549 Å, $Ly_\alpha\lambda$1216 Å (the last two lines are not detected in the sources of this work).

To measure spectroscopic redshifts, emission and absorption lines were identified, and their observed-frame wavelengths using Gaussian profile fitting was estimated. To determine the redshift solution, we cross match the wavelength ratios of the identified lines

with a look-up table of wavelength ratios based on the emission and absorption lines observed in AGN and galaxy spectra. For the large majority of cases there are multiple lines detected, and there is only one valid redshift solution. There are only two sources where the redshift is based on a single line identification (marked with "quality B" flags in Table 3.1). The lines identified for each individual source are tabulated in Table 3.1. At the end, the definition for redshift is given by the shift in the wavelength (λ) of the object's spectrum towards the red side, as per the following equation (equation 3.1), is used to obtain the definitive measurements.

$$z + 1 = \frac{\lambda_{observed}}{\lambda_{emitted}}. \tag{3.1}$$

The total number of sources with spectroscopic redshift measurements and classifications is 35. While these account for only 13% of the overall spectroscopically identified sample from the *NuSTAR* Serendipitous survey, they form a larger percentage ($\approx 20\%$) of the optically faint sample from the same catalog.

The 35 sources with identify emission lines and redshifts were classified, based purely on the optical spectra, as follows:
(1) Extragalactic sources with identified lines. Both permitted emission lines (e.g., the Balmer series and MgII) and forbidden (e.g., [OIII] and [NII]) ones. These sources are further sub-classified into two,
(1.a) BLAGN - sources with permitted line broader than the forbidden. There are 7 sources out of 30 extragalactic ones, where only permitted or semiforbidden emission lines are identified. The line profiles are visually broad. Also, these sources predominantly lie at higher redshifts, at z $\gtrsim$ 0.9 (see figure 3.1). These Magellan/Gemini-S sources span a range in redshift between $\approx 0.9 - 2.2$ and most are faint in the optical ($< R >= 20.4$ mag).
(1.b) NLAGN - the remaining 23 out of 30 sources, with only forbidden line detections and Balmer lines. See Table 3.1 for the classification. These sources are the obscured AGN in the unified model (Antonucci, 1993) viewed edge-on. In earlier studies of the lower-z universe, line ratios such as [OIII] λ5007/H_β, [NII] λ6583/H_α, etc., have been used to differentiate spectra that show narrow lines due to ionization by hot stars from spectra that show narrow lines due to an active nucleus (e.g., Veilleux & Osterbrock, 1987). We do not measure such line ratios or apply them in the classification, due to our spectral and spatial resolutions are too low to deblend and measure ratios accurately. .
(2) Galactic sources, emission and absorption lines are detected in all the stars. In particular, they all have Balmer series emission lines, and the majority of sources has CaII absorption line. This makes us think that these five Galactic sources are indeed

High Mass X-ray Binaries (HMXB, Reig, 2004). Tomsick et al. (in prep.) will present a detailed analysis of the Galactic subsample of the *NuSTAR* Serendipitous survey.

The two sources where the redshift is based on a single line identification are NGC1313_X1X2_s1 and NGC1365_s3. The emission line detected in these sources is identified as MgII λ2800 Å. In those cases this is well justified: MgII is a dominant broad line in quasar spectra, and there is a relatively large separation in wavelength between the next strong line bluewards of MgII, like CIII] λ1909 Å, and that redwards of MgII, like Hβ λ4861 Å. Although in some cases (MCG_01_24_012_sA5, PDS456_s1, 3C279_sA01133, Kepler_s1) it can be seen that MgII accompanied by CIII] or HeII line, making a more reliable redshift measurements. This means that MgII can be observed in isolation for redshifts of z $\sim$ 0.8 in cases where our wavelength coverage is slightly narrower than the usual, or if other lines (e.g., CIII] and H_β) are below the detection threshold. MgII can also be distinguished in higher S/N data due to the shape of the neighboring FeII pseudo-continuum.

Thus, considering the total classified sample, the majority of the sources (23 or 65.7%) are NLAGNs, 7 (20%) are BLAGNs and the remaining 5 (14.3%) are galactic objects (e.g., HMXB). Table 3.1 shows the following for all Magellan/Gemini-S Serendipitous sources with optical spectra: the *R*-magnitude, the spectroscopic redshift, the optical classification and the identified emission/absorption lines.

Figure 3.1 presents the scatter plot of the *R*-band magnitude versus the redshift revealing how the source composition changes as a function of redshift for the entire sample, i.e. L16 sources, which have an identified optical counterpart. In color, the sources observed using the instruments described above are highlighted in blue, cyan and yellow. From the dotted line $R = 20$ and upwards we distinguish the fainter sources, and those on other side its the contrary from the dotted line and below. The range of *R*-band magnitude for the sources studied in this thesis is $\approx 14 - 22$ mag. In comparison to L16 is easly distinguishable that 12 Magellan/Gemini-S sources belong to the "fainter" region.

If we just concentrate on our sample, the redshifts for the extragalactic sources cover a large range, from $z = 0.0867$ to 2.242. For these objects with independent detections in the high-energy band (8−24 keV), to which *NuSTAR* is uniquely sensitive, the median redshift is $< z > = 0.612$. There is a significant bias towards BLAGNs at higher redshifts; here it is noticed that more sources are identified as NLAGN. This was also found for the *NuSTAR* surveys in well-studied fields (e.g., Civano et al., 2015), and for surveys with sensitive lower energy (< 10 keV) X-ray observatories such as the *Chandra* and the *XMM-Newton* (e.g., Barger et al., 2003; Eckart et al., 2006). This effect is largely due to the selection biases against the detection of highly absorbed AGNs, and against the spectroscopic identification of the optically fainter NLAGNs (e.g., Treister et al., 2004).

Also, most of the high redshift sources are broad line AGN, with a redshift up to 2.242. These ones also have fainter optical counterparts with optical magnitudes in the $19 - 22$ range. For the lower redshift region we see that the NLAGN is the dominant class in a range of magnitude between $18 - 22$ with a median redshift up to 0.75.

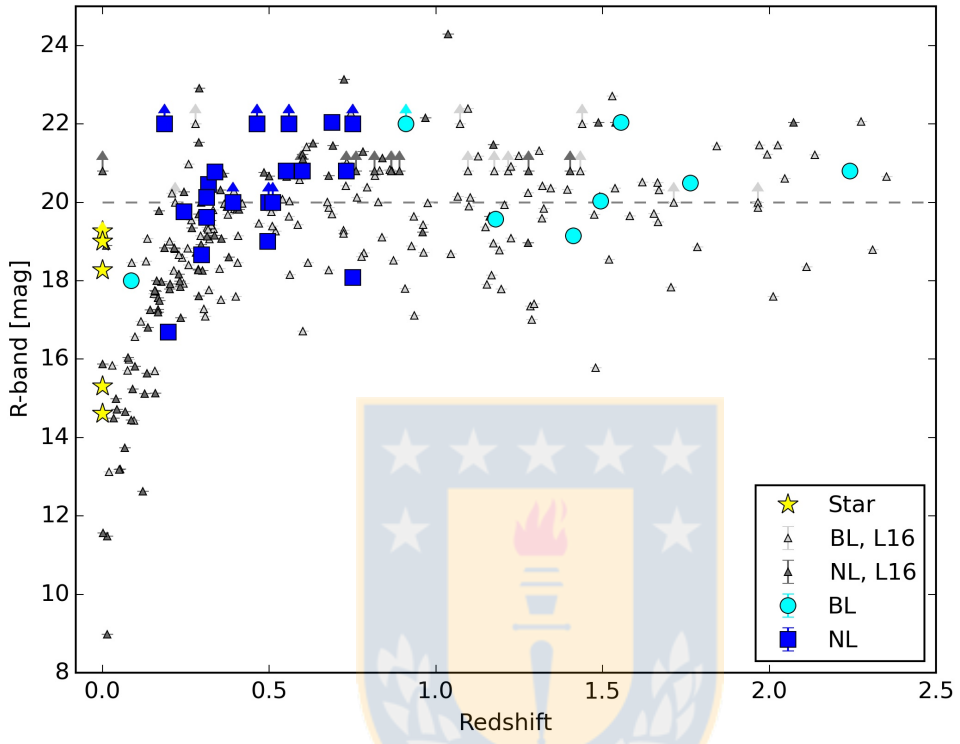

FIGURE 3.1: *R*-band magnitude versus redshift for sources with spectroscopic identification in this work compared with L16.

TABLE 3.1: Spectroscopic Properties

Source Name[a]	R-Mag[b]	Redshift[c]	Quality[d]	Type[e]	Emission[f]	Absorption[f]
1E1048d1m5937 s1	14.61	0.000	A	Galactic	H_ϵ H_δ H_γ H_β H_α	NaD
1H0707m495s1	19.15	1.412	A	BLAGN	CIII] MgII	
3C279 sA01133	20.49	1.767	A	BLAGN	CIII] MgII	
BULLET BULLET SHOCK s1	18.67	0.297	A	NLAGN	H_β [OIII] H_α [NII]	
ESO416 G002 s4	20.12	0.313	A	NLAGN	H_β [OIII] H_α [NII]	
FAIR ALL 0272 sA3	19.62	0.313	A	NLAGN	[OII] [OIII] H_α [NII]	
GRB130925A s1	>22	0.751	A	NLAGN	[OII] H_β [OIII]	
HLX 1 s4	>19	0.495	A	NLAGN	[OII] H_γ H_β [OIII]	$Ca_{H\&K}$
IGRJ14552m5133 s1	>22	0.186	A	NLAGN	H_β [OIII] H_α [NII] [SII]	
IRAS 12071m0444 s1	>20	0.391	A	NLAGN	H_β [OIII] [OI] H_α [NII]	H_δ
Kepler s1	20.8	2.242	A	BLAGN	HeII MgII	
MCG 01 24 012 sA5	20.03	1.493	B	BLAGN	CIII] MgII	
MRK1210 sA2	-	0.000	A	Galactic	H_δ H_γ H_β HeI H_α	MgIb FeI NaD
NGC1313 X1X2 s1	19.57	1.180	B	BLAGN	MgII	
NGC1313 X1X2 s2	>20	0.391	A	NLAGN	[OIII] H_α [NII]	
NGC1365 s1	>22	0.559	A	NLAGN	[OII] H_β [OIII]	
NGC1365 s3	>22	0.910	B	BLAGN	MgII	
NGC3256 s1	>20	0.498	A	NLAGN	[OII] H_β [OIII] H_α [NII]	
NGC4945 sA01142	18.085	0.751	B	NLAGN	[OII] H_ϵ HeII	
NGC4945 sA01146	-	0.511	C	NLAGN	H_δ HeII H_β [OIII]	
NGC5728 s1	20.8	0.593	A	NLAGN	[OII] [OIII]	
NGC7582 s1	>22	0.468	A	NLAGN	[OII] H_β [OIII]	
PDS456 s1	22.04	1.555	B	BLAGN	CIII] MgII	
PDS456 s2	16.69	0.197	A	NLAGN	[OIII] H_α [NII]	
PDS456 s6	22.04	0.688	A	NLAGN	[OII] H_γ H_β [OIII]	
PG1211p143 sA6	>19	0.000	A	Galactic	H_γ H_β H_α	FeI NaD CaI CaII
PG1211p143 sA01134	20.45	0.318	A	NLAGN	H_β [OIII] H_α [NII] [SII]	
PG1211p143 sA01148	>19	0.245	B	NLAGN	H_γ H_β [OIII] H_α [NII] [SII]	$Ca_{H\&K}$
PG1211p143 sA011411	18.27	0.000	A	Galactic	H_γ H_β H_α	MgI FeI NaD CaII
PKS1552m331 FIELD s1	20.8	0.551	A	NLAGN	[OII] H_β [OIII]	
PSRJ1023p0038 sA01142	19.26	0.000	A	Galactic	H_β H_α CaII	FeI NaD NaI
PSRJ0437m4715 s4	20.8	0.731	A	NLAGN	H_γ HeII H_β [OIII]	
PSRJ0437m4715 s5	20.77	0.337	B	NLAGN	[OII] H_β H_α [NII]	
SUPER ANTENNAE sA5	>18	0.559	A	NLAGN	[OII] [OIII]	
Vela X1 s1	20.8	0.0867	A	BLAGN	H_β [OIII] [OI] H_α [NII]	

Notes.
[a] Name of the *NuSTAR* Serendipitous source. [b] *R*-band magnitude of the optical counterpart. [c] Optical spectroscopic redshift. [e] Optical spectroscopic classification. [f] Emission/absorption detected lines.
Table prepared in this work.

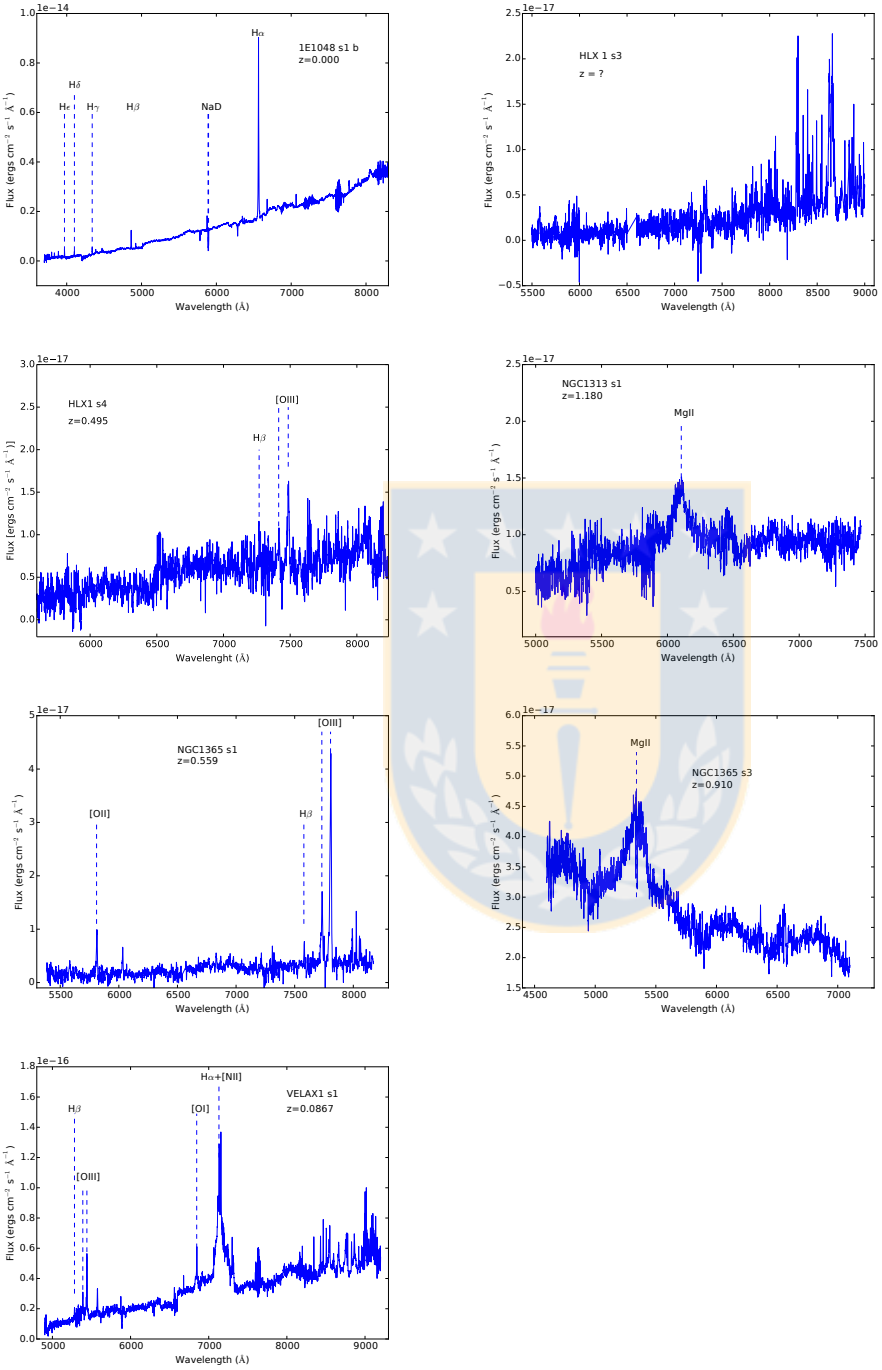

FIGURE 3.2: MagE spectra of the run 1; own elaboration.

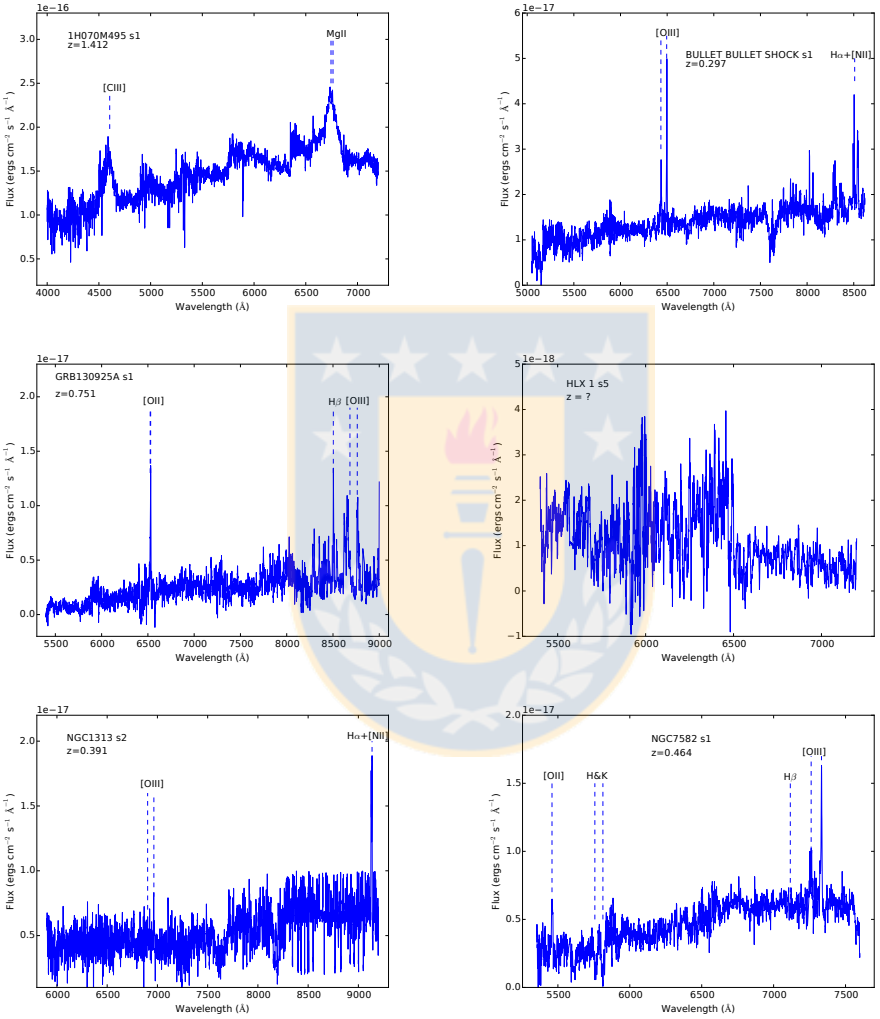

FIGURE 3.3: MagE spectra of the run 2; own elaboration.

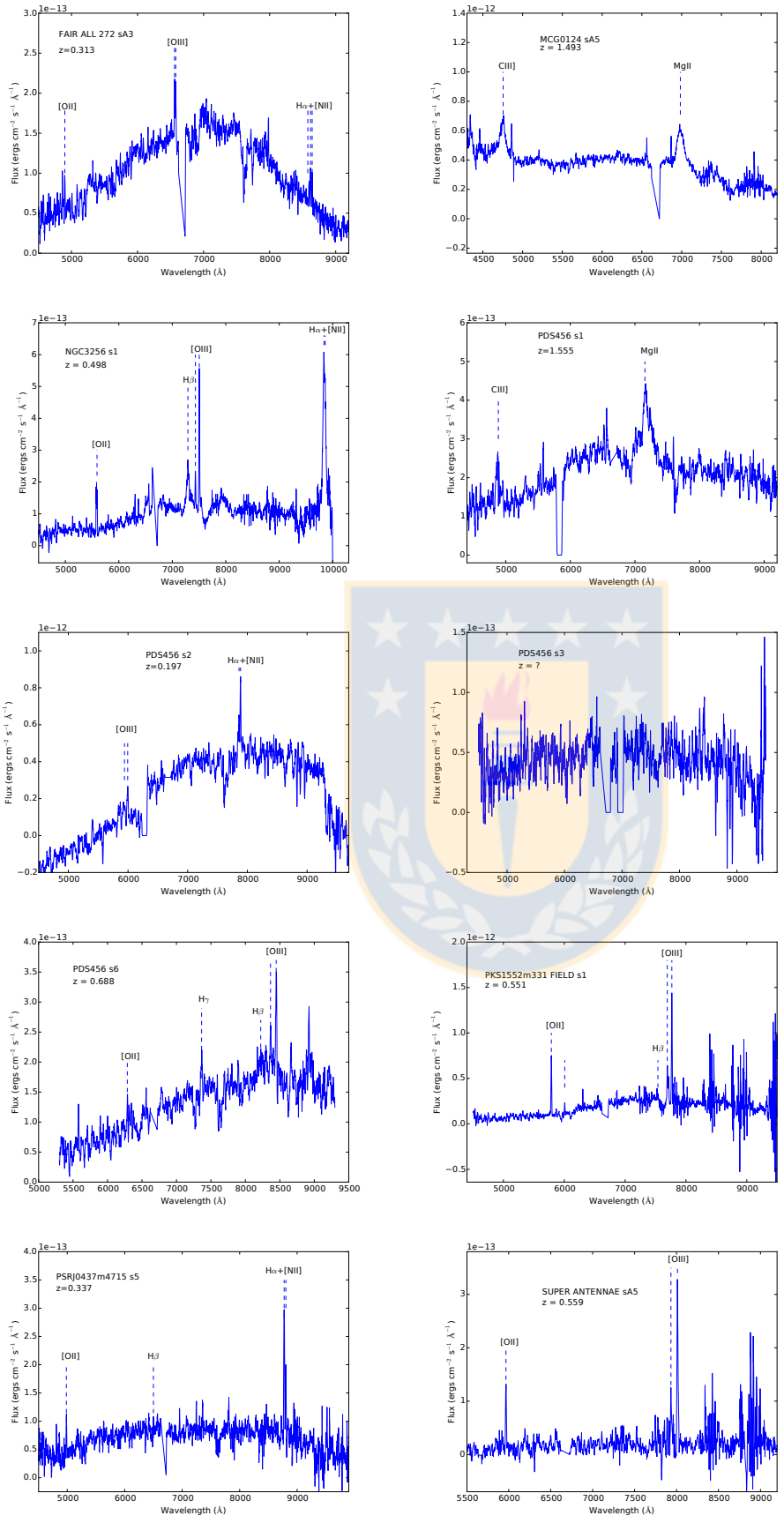

FIGURE 3.4: IMACS spectra of the run 3; own elaboration.

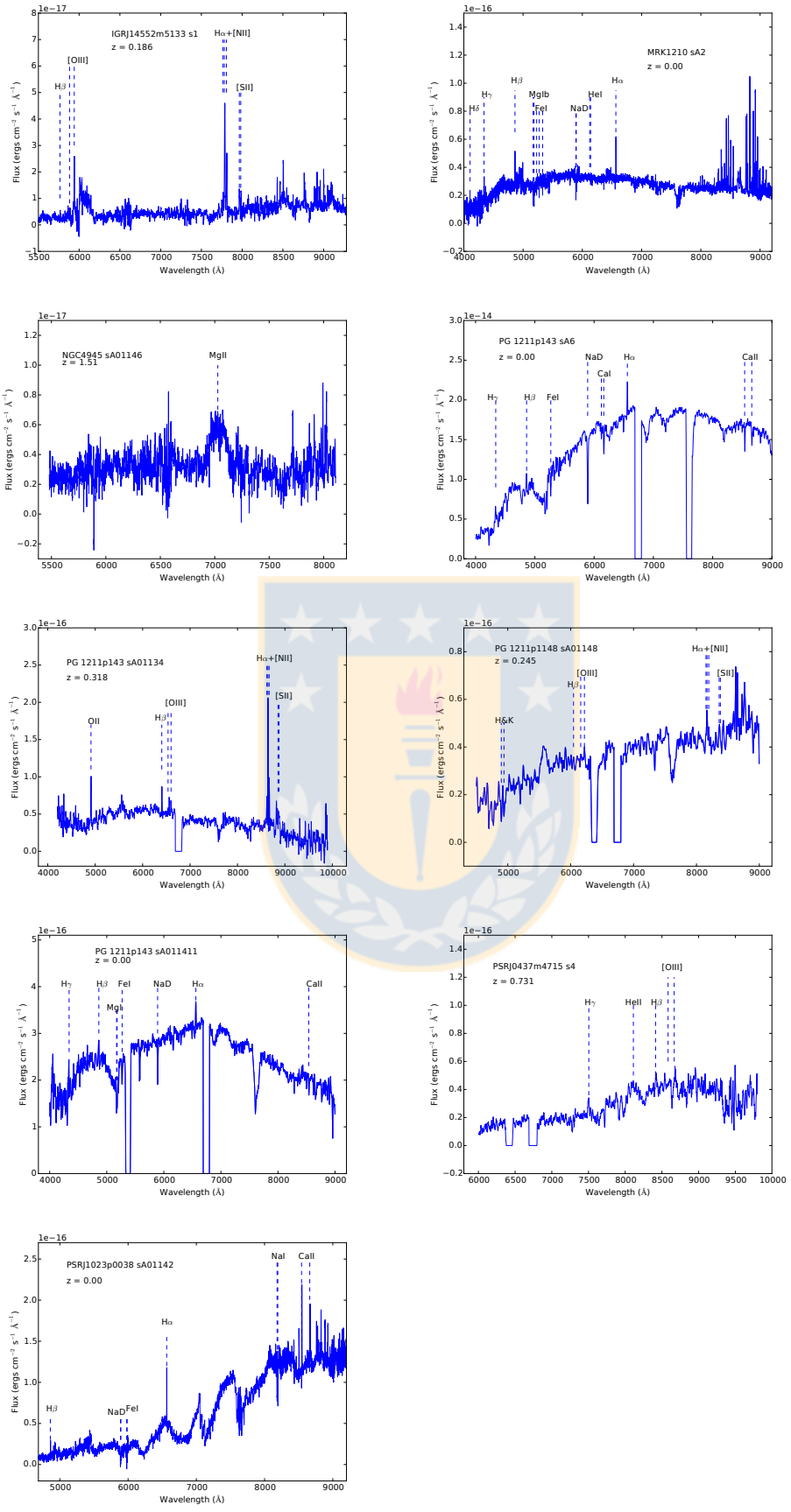

FIGURE 3.5: MagE and IMACS spectra of the run 4; own elaboration.

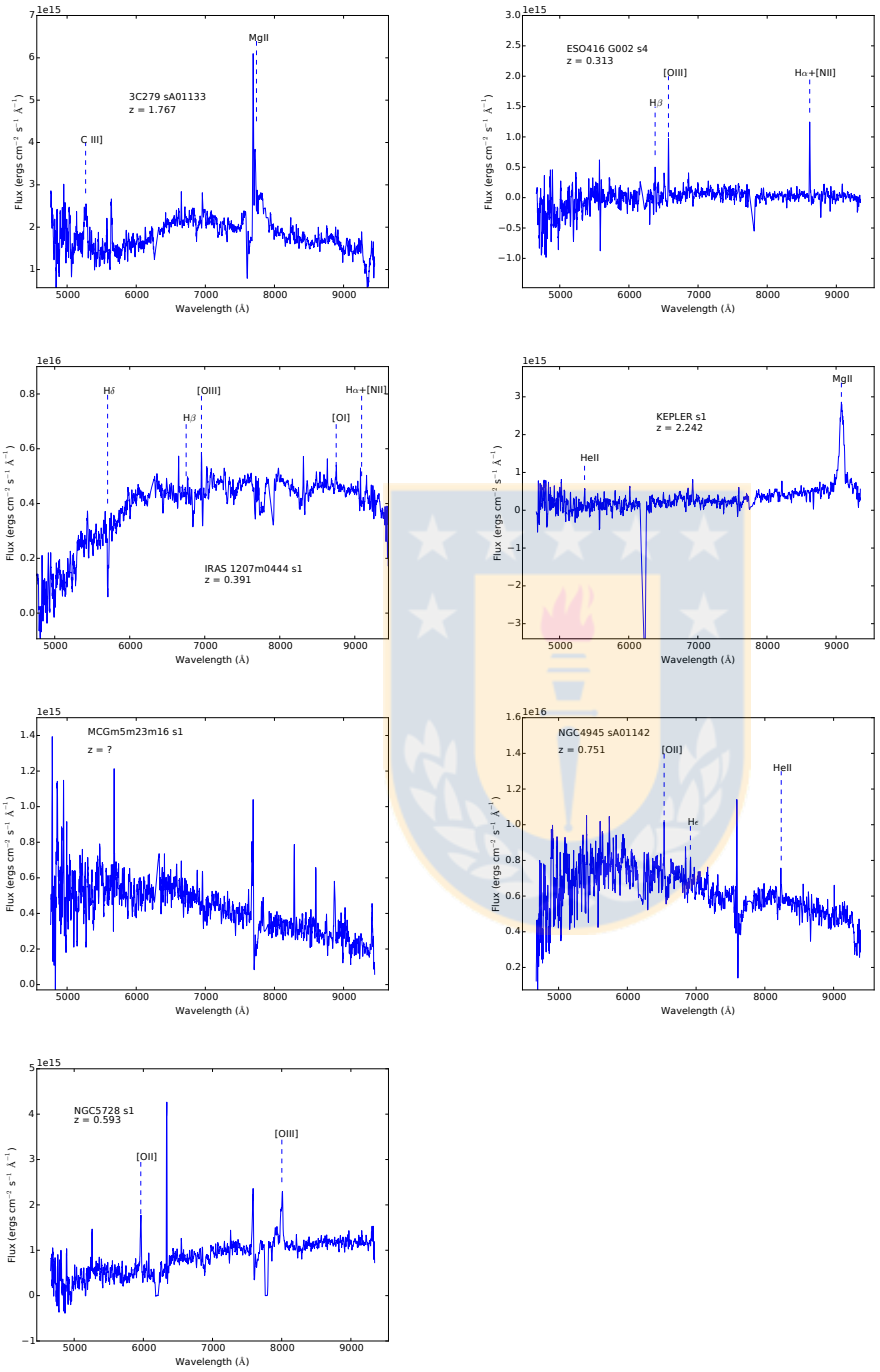

FIGURE 3.6: GMOS spectra of the run 5; own elaboration.

Chapter 4

Multiwavelength Data

4.1 X-ray Properties

Each source detected by *NuSTAR* Serendipitous survey, was compiled by L16. In this chapter, we will discuss the X-ray characteristics for the sources studied in their work. The results of the X-ray reduction is important for the subsequent analysis of the data.

Images have been extracted in the spectral bands, $3-24$ (total), $3-8$ (soft) and $8-24$ (hard) keV for both focal plane modules (FPM) from *NuSTAR*.

The net counts, count rates and fluxes was measured by L16 from which they also obtained the rest-frame luminosities. Table 4.1 show the results for the sample studied in this thesis. For the aperture photometry, they adopt a circular aperture of 30" radius to measure the gross (i.e., source plus background) counts (S), and subtracted S from the scaled background counts in order to obtain the net source counts (S_{net}). The errors on S_{net} are computed as $1+\sqrt{S+0.75}$ (84% confidence level; e.g. Gehrels, 1986). For sources undetected in a given band, upper limits for S_{net} are calculated using the Bayesian approach outlined in Kraft, Burrows, & Nousek (1991). To determine the net count rate, they divide S_{net} by the exposure time drawn from the vignetting-corrected exposure map (mean value within the 30" aperture).

To measure fluxes, L16 convert the deblended 30" count rates using the following factors: 6.7×10^{-11}, 9.4×10^{-11} and 13.9×10^{-11} erg cm^{-2} cts^{-1} for the soft, full and hard X-ray bands, respectively. These conversion factors were derived to account for the *NuSTAR* response, and assume an unabsorbed power-law with a photon index of $\Gamma_{eff}=1.8$ (typical of AGN detected by *NuSTAR*; e.g., Alexander et al., 2013). The conversion factors return aperture-corrected fluxes; i.e., they are corrected to the 100% encircled-energy fraction of the PSF. The rest-frame $10-40$ keV luminosity was determined by

extrapolating from a measured observed-frame flux, assuming a photon index of $\Gamma_{eff} = 1.8$. To ensure that the adopted observed-frame flux energy band corresponds to the rest-frame $10 - 40$ keV one, they use the observed-frame $8 - 24$ and $3 - 8$ keV bands for sources with redshifts of $z < 1.35$ and $z \geqslant 1.35$, respectively. For cases with a non-detection in the relevant band (i.e., $8 - 24$ or $3 - 8$ keV), they extrapolate from the full band ($3 - 24$ keV).

For our sample, there are only 13 detection in the 8−24 keV band, which is unique to *NuSTAR* amongst focusing X-ray observatories. The net (cleaned, vignetting-corrected) exposure times per source (t_{net}; for the combined FPMA+B data) have a large range of values, from 17−350 ks, with a median of 60 ks. For the 3−8, 8−24, and 3−24 keV bands, the lowest net source counts (S_{net}) for sources with detections in these bands are 25, 17, and 31, respectively, and correspond to one individual source ESO416-G002 s4. The highest S_{net} values are 351, 191, and 546 net source counts, respectively. The median S_{net} values are 73, 94, and 241, respectively.

These 13 sources that were detected in the hard X-ray band, is assumed to have a very hard X-ray spectrum. This combined with the fact that they being very faint in the optical bands ($R > 18$ mag) makes them good candidates to be obscured AGN.

4.2 Ultraviolet to Mid-Infrared Photometry

To further quantify the brightness of the sources we used Ultraviolet (UV) to Mid-Infrared (MIR) data.

Table 4.2 presents the broad-band UV-MIR photometric properties of the Magellan/Gemini-S sources. We obtained them from existing, publicly available all-sky or large-area surveys, including the Galaxy Evolution Explorer Martin et al. (GALEX; 2005), the Wide-field Infrared Survey Explorer (WISE; Wright et al., 2010), the Two Micron All Sky Survey (2MASS; Skrutskie et al., 2006) and the mid-IR IRAC observations of *Spitzer* (A. Melo in prep.). The source photometry is provided in its native format for all the sources.

For 60% of the sources we don't find a reliable optical counterpart and thus making their photometry uncertain. One option to circumvent this problem is by crossmatching the *Spitzer* with the *Chandra*/*XMM-Newton* data to obtain the accurate position of the source (A. Melo in prep.), and thus, have the correct magnitudes of them in the different bands. But still, there are some sources (3) that needs more deep observations. The

TABLE 4.1: *NuSTAR* sources properties

Source Name[a]	Target Field (NuSTAR J)[b]	RA[c]	Dec[c]	3-24 keV[d]	3-8 keV[d]	8-24 keV[d]	Flux $\times 10^{14}$ (3-24keV)[e]	Flux $\times 10^{14}$ (3-8keV)[e]	Flux $\times 10^{14}$ (8-24keV)[e]
1E1048d1m5937 s1	105008-5958.8	10:50:08.68	-59:58:53.2	240.91±40.29	164.66±30.16	78.08±27.16	3.15±0.58	3.75±1.303	7.69±1.29
1H0707m495 s1	070859-4937.9	07:08:59.59	-49:37:58.1	169.16±27.49	90.04±20.02	80.28±19.51	2.97±0.66	6.35±1.54	9.0049±1.4634
3C279 sA01133	125617-0543.8	12:56:17.22	-05:43:48.4	61.16±19.103	<72.36	<29.39	<4.02	<3.55	4.99±1.56
Bullet Bullet shock s1	065843-5550.2	06:58:43.23	-55:50:17.3	293.27±33.48	142.78±23.89	150.90±24.17	3.01±0.50	7.88±1.26	10.36±1.18
ESO416 G002 s4	023448-2936.6	02:34:48.29	-29:36:36.3	31.88±12.39	25.29±8.84	< fill	6.38±2.23	<11.77	14.059±5.465
FAIR ALL 0272 sA3	082303-0502.7	08:23:03.32	-05:02:47.4	39.19±10.53	<18.91	30.13±8.33	<5.89	23.95±6.62	21.082±5.66
GRB130925A s1	024507-2605.7	02:45:07.63	-26:05:47.9	140.21±25.81	99.75±18.71	<72.22	2.74±0.51	<4.93	6.474±1.19
HLX 1 s4	011103-4602.7	01:11:03.50	-46:02:44.8	90.81±23.29	< 76.40	<69.42	<3.27	<7.21	6.38±1.64
IGJR14552m5133 s1	-	14:54:39.69	-51:35:21.8	–	–	<23.87	6.67±1.92	<13.85	15.81±4.05
IRAS 12071m0444 s1	031924-6629.9	03:19:24.45	-66:29:58.0	159.44±28.65	85.44±19.86	73.33±21.27	1.95±0.45	3.92±1.14	5.77±1.037
Kepler s1	173035-2133.8	17:30:35.28	-21:33:50.4	646.41±40.76	396.21±32.04	251.67±25.93	8.14±0.66	12.46±1.28	20.89±1.32
MCG 01_24_012 sA5	092042-0808.9	09:20:42.19	-08:08:57.6	56.64±17.27	48.09 ±13.36	<24.64	3.49±0.97	<4.31	6.69±2.042
MRK1210 sA2	080421+0504.9	08:03:59.97	+05:13:04.4	–	–	–	<10.83	<19.84	18.99 ± 5.21
NGC1313 X1X2 s1	031901-6629.7	03:19:01.84	-66:29:46.2	117.62±27.47	78.66±19.59	<70.13	1.44±0.36	<2.76	3.12±0.73
NGC1313 X1X2 s2	031924-6629.9	03:19:24.45	-66:29:58.0	159.44±28.65	85.93±19.86	73.33±21.27	1.95±0.45	3.92±1.14	5.77±1.037
NGC1365 s1	033342-3613.9	03:33:42.26	-36:13:58.4	459.75±48.49	270.09 ±34.65	191.65±34.43	4.83±0.62	8.82±1.58	14.078±1.485
NGC1365 s3	033406-3603.9	03:34:06.35	-36:03:58.2	100.55±17.14	57.32±12.57	43.55±12.01	6.20±1.36	12.62±3.48	19.39±3.31
NGC3256 s1	102710-4352.5	10:27:10.68	-43:52:31.3	160.41±26.15	88.078±19.35	<101.28	3.34±0.73	<9.87	10.32±1.68
NGC4945 sA01142	130519-4934.2	13:05:19.54	-49:34:13.5	57.39±17.84	<54.48	<42.70	<3.99	<77.39	7.039±2.189
NGC4945 sA01146	–	13:06:08.53	-49:31:35.7	–	–	–	–	–	–
NGC5728 s1	144238-1709.8	14:42:38.23	-17:09:52.7	56.98±12.03	45.15±9.65	<24.67	9.86±2.11	<1.29	20.087±4.243
NGC7582 s1	231840-4223.0	23:18:40.47	-42:23:04.4	46.73±12.91	<27.16	32.94±10.31	<4.14	11.16±3.49	10.71±2.96
PDS456 s1	172803-1423.0	17:28:03.98	-14:23:04.8	184.99±26.39	119.45±19.54	<95.73	4.89±0.80	<9.99	13.079±1.866
PDS456 s2	172805-1420.9	17:28:05.85	-14:20:59.4	166.99±25.99	82.22±18.05	<85.029	<3.045	6.14±1.65	7.72±1.51
PDS456 s6	172822-1421.4	17:28:22.84	-14:21:25.0	–	–	–	–	–	–
PG1211p143 sA6	–	12:14:42.09	+14:10:24.4	–	–	–	–	–	–
PG1211p143 sA01134	121415+1408.1	12:14:15.55	+14:08:09.3	77.0702±27.61	<73.14	<66.795	<1.62	<3.49	2.73±0.97
PG1211p143 sA01148	121357+1407.3	12:13:57.13	+14:07:22.5	–	–	–	<10.83	<5.69	4.64±1.17
PG1211p143 sA011411	121435+1404.5	12:14:35.99	+14:04:30.5	71.71±27.55	<42.46	<88.69	<0.89	<4.52	2.45±0.94
PKS1552m331 FIELD s1	155520-3315.1	15:55:20.00	-33:15:11.8	109.89±18.64	74.63±13.67	37.95±12.99	8.18±1.49	9.39±3.22	18.086±3.067
PSRJ1023p0038 sA01142	102318+0036.5	10:23:18.11	+00:36:34.7	38.048±15.86	<33.50	<41.45	<2.45	<7.61	4.73±1.97
PSRJ0437m4715 s4	043750-4715.0	04:37:50.94	-47:15:04.6	103.047±28.16	<93.13	<73.16	<2.59	<5.05	4.67±1.28
PSRJ0437m4715 s5	043754-4716.0	04:37:54.08	-47:16:05.7	201.47±43.15	85.46±30.49	104.93±30.99	2.12±0.76	6.98±2.06	8.68±1.86
SUPER ANTENNAE sA5	193241-7242.4	19:32:41.62	-72:42:25.0	63.21±16.68	<93.13	<67.48	<2.4±8	<12.79	8.11±2.14
VELA X1 s1	090223-4039.4	09:02:23.99	-40:39:25.5	546.62±36.74	351.82±28.50	185.65±23.63	55.601±4.504	76.74±9.77	150.34±10.11

Note.

[a] Unique *NuSTAR* source name. [b] Unique source identification number (ID), based on the counts-weighted *NuSTAR* source position adjusted to an appropriate level of precision (based on the *NuSTAR* positional accuracy), using the International Astronomical Union (IAU) approved naming convention for *NuSTAR* sources: *NuSTAR* JHHMMSS±DDMM.m, where m is the truncated fraction of an arcminute in declination for the arcseconds component. [c] Right ascension (R.A.) and declination (Dec.). [d] Net counts for *NuSTAR* source position in the $3-24$ keV, $3-8$ keV and $8-24$ keV bands. Units: s^{-1}. [e] The observed-frame fluxes and associated errors (84% CL) for the three standard energy bands, after deblending has been performed. These are aperture corrected values (i.e., they correspond to the full *NuSTAR* PSF). Units: erg s^{-1} cm^{-2}.

The − means that the measurements in these sources were not able to obtained in the final catalog from L16.

data obtained in this section (Table 4.2) are not sufficient for a complete photometric analysis.

Table 4.2: Ultraviolet-Mid-Infrared Sources Properties

ID (XMM)			GALEX		WISE				2MASS		
Source Name[a]	RA[b]	Dec[b]	FUV[c]	NUV[c]	W1[d]	W2[d]	W3[d]	W4[d]	J[e]	H[e]	K[e]
1H0707m495 s1	07:08:59.80	-49:37:54.0	–	–	15.57 ± 0.03	14.48 ± 0.03	11.84 ± 0.15	9.03 ± 0.31	–	–	–
3C279 sA01133	12:56:16.39	-05:43:55.5	–	21.93 ± 0.45	17.08 ± 0.12	16.08 ± 0.19	12.15 ± 2.00	9.09 ± 2.00	–	–	–
Bullet_shock s1	06:58:43.74	-55:50:20.0	–	–	15.12 ± 0.03	14.79 ± 0.04	12.39 ± 0.25	8.91 ± 2.00	–	–	–
ESO416_G002 s4	02:34:48.72	-29:36:25.5	–	22.29 ± 0.39	14.93 ± 0.03	14.26 ± 0.04	11.76 ± 0.20	8.77 ± 2.00	–	–	–
FAIR_ALL_0272 sA3	08:23:03.07	-05:02:51.9	–	–	15.29 ± 0.04	14.72 ± 0.06	12.06 ± 0.36	9.08 ± 2.00	–	–	–
GRB130925A s1	02:45:08.46	-26:05:52.6	–	–	17.61 ± 0.14	16.52 ± 0.20	12.67 ± 0.38	9.37 ± 2.00	–	–	–
HLX1 s4	01:11:03.92	-46:03:04.0	21.96 ± 0.07	21.09 ± 0.03	16.08 ± 0.06	15.91 ± 0.14	12.66 ± 2.00	8.70 ± 2.00	–	–	–
IGRJ14552m5133 s1	14:54:40.60	-51:35:15.5	–	–	14.34 ± 0.05	13.22 ± 0.04	9.813 ± 0.05	7.17 ± 0.13	16.95	16.57	15.25
IRAS_12071m0444 s1	–	–	–	–	–	–	–	–	–	–	–
Kepler s1	17:30:34.89	-21:33:42.7	–	–	–	–	–	–	–	–	–
MCG_01_24_012 sA5	09:20:42.97	-08:08:59.9	–	–	16.67 ± 0.09	15.24 ± 0.09	11.78 ± 2.00	8.56 ± 2.00	–	–	–
NGC1313_X1X2 s1	03:19:01.49	-66:29:32.5	–	–	15.72 ± 0.039	14.62 ± 0.04	11.88 ± 0.18	8.81 ± 0.28	–	–	–
NGC1313_X1X2 s2	03:19:25.53	-66:29:54.2	–	–	–	–	–	–	–	–	–
NGC1365 s1	03:33:42.93	-36:14:02.2	–	22.53 ± 0.41	15.25 ± 0.03	14.19 ± 0.03	11.17 ± 0.08	8.30 ± 0.15	–	–	–
NGC1365 s3	03:34:07.49	-36:04:01.8	–	21.23 ± 0.07	15.71 ± 0.04	14.72 ± 0.05	12.54 ± 0.29	9.61 ± 2.00	–	–	–
NGC4945 sA01142	13:05:20.77	-49:34:08.4	–	–	16.33 ± 0.054	17.50 ± 0.51	12.96 ± 2.00	9.32 ± 2.00	–	–	–
NGC4945 sA01146	13:06:08.43	-49:32:02.4	–	–	–	–	–	–	–	–	–
NGC5728 s1	14:42:39.58	-17:10:00.3	–	–	–	–	–	–	–	–	–
NGC7582 s1	23:18:40.89	-42:23:00.9	22.62 ± 0.15	21.37 ± 0.08	15.72 ± 0.04	15.29 ± 0.08	12.48 ± 0.38	8.67 ± 2.00	–	–	–
PDS456 s1	17:28:04.62	-14:23:05.6	–	–	–	–	–	–	15.48 ± 0.12	15.054 ± 0.075	14.34 ± 0.18
PDS456 s2	17:28:05.70	-14:21:09.3	–	–	11.02 ± 0.023	11.08 ± 0.021	10.75 ± 0.11	8.26 ± 2.00	12.08 ± 0.03	11.39 ± 0.03	11.19 ± 0.026
PDS456 s6	17:28:22.83	-14:21:25.2	–	–	15.47 ± 0.07	14.56 ± 0.08	11.52 ± 0.19	8.91 ± 2.00	–	–	–
PG1211p143 sA01134	12:14:15.98	+14:08:13.6	–	23.49 ± 0.60	16.57 ± 0.08	15.67 ± 0.15	11.66 ± 2.00	9.04± 2.00	–	–	–
PG1211p143 sA01148	12:13:57.73	+14:07:09.9	23.77 ± 0.20	23.36 ± 0.20	15.80 ± 0.05	15.33 ± 0.09	12.33 ± 2.00	9.01 ± 2.00	–	–	–
PKS1552m331_FIELD s1	15:55:19.55	-33:15:10.6	–	–	15.24 ± 0.05	15.04± 0.08	12.27 ± 2.00	8.77 ± 2.00	–	–	–
PSRJ0437m4715 s4	04:37:51.39	-47:15:03.7	–	–	15.87 ± 0.04	15.52 ± 0.07	13.12 ± 2.00	9.31 ± 2.00	–	–	–
PSRJ0437m4715 s5	04:37:54.16	-47:15:51.6	–	22.27 ± 0.62	15.52 ± 0.04	14.83 ± 0.05	11.08 ± 0.09	8.75 ± 0.30	–	–	–
SUPER_ANTENNAE sA5	19:32:41.88	-72:42:34.3	–	–	–	–	–	–	–	–	–
Vela_X1 s1	09:02:24.15	-40:39:29.2	–	–	12.91 ± 0.02	12.31 ± 0.02	10.18 ± 0.05	8.27 ± 0.28	15.76 ± 0.09	14.69 ± 0.09	13.94 ± 0.07

Note.
Source photometry given by every catalogs. [a] Source name. [b] Counterpart source position. Source photometry given in its native format: [c] AB mag for GALEX, Vega mag for [d] WISE and for [e] 2MASS.

Chapter 5

Analysis and Results

5.1 Redshifts and Luminosities

The X-ray emission is a common characteristic to all AGN (Elvis et al., 1978), with similar properties in the whole wide range of observed luminosity (X-ray luminosity of AGN varies from $L_X \sim 10^{42-48}$ erg s^{-1}). Estimating the bolometric luminosity of AGN is not easy, because in most cases observations are available only in selected energy bands. In this case the best band to use is probably the hard X-ray band, where the effect due to absorption is negligible, at least for Compton thin objects – X-ray surveys are widely used to study AGN population (Esposito V., 2016).

It is clear that the kind of X-ray sources identified in surveys depend directly on the depth of the optical spectroscopy follow-up. For example, unobscured AGN are bright in the optical bands, therefore in surveys with shallow optical follow-up unobscured AGN are mostly detected (e.g., Georgantopoulos et al., 1996). On the other hand, deep X-ray coverage, together with an extensive spectroscopy campaign, allows us to detect more faint optical counterparts. Therefore, the population in very deep surveys is dominated by obscured AGN (e.g., L16).

In Figure 5.1 we show the rest-frame $10-40$ keV luminosity versus the redshift for the 30 identified sources as extragalactic. We also compare our results to those detected in the *Swift*-BAT survey (Burlon et al., 2011, in diamond), *NuSTAR* Serendipitous survey (the first 10 from Alexander et al. (2013) in green triangles and those from L16 are shown in gray triangles). The cyan circles and blue square are the sources presented in this work. The darker colours are for BLAGNs and the other are for NLAGNs. The gray dashed line in Figure 5.1 shows the detection limit for X-ray sources in *Swift*-BAT and *NuSTAR* survey.

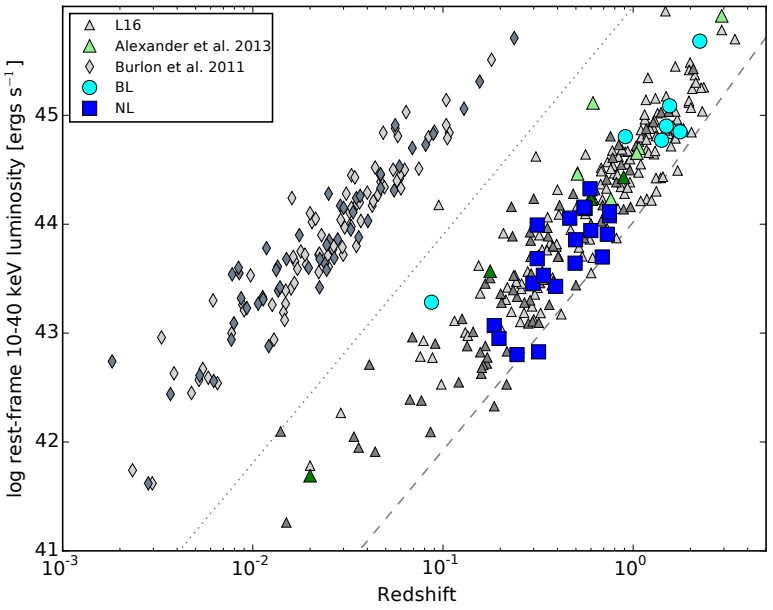

FIGURE 5.1: Rest-frame 10−40 keV luminosity ($L_{10-40keV}$) versus redshift, for this work

The luminosities are calculated by L16 from the observed frame *NuSTAR* fluxes, assuming an effective photon index of $\Gamma_{eff} = 1.8$. The *NuSTAR* Serendipitous survey covers a large range in $10 - 40$ keV luminosity; the large majority of the unassociated sources lie in the range of $L_{10-40\ \mathrm{keV}} \sim 10^{42-46}$ erg s^{-1}. The mean luminosity of $L_{10-40\ \mathrm{keV}} \approx 1.2 \times 10^{44}$ erg s^{-1} shows us that the *NuSTAR* Serendipitous sources are more luminous than the vast majority of the *Swift*-BAT AGNs, where the median luminosity value of the *Swift*-BAT AGNs is $L_{10-40\ \mathrm{keV}} \approx 3 \times 10^{43}$ erg s^{-1}. The larger fraction of luminous AGNs detected by *NuSTAR*, in comparison to *Swift*-BAT, is a direct consequence of the higher sensitivity of *NuSTAR* (Alexander et al., 2013).

It is important to describe the Magellan/Gemini-S sources. The range of redshifts for sources in this sample is large, from galactic sources at z = 0 to a source at z= 2.242. The source with the highest-redshift is Kepler s1, an optically classified source like BLAGN with a $L_{10-40\ \mathrm{keV}} = 4.79 \times 10^{45}$ erg s^{-1}, is also the brightest in X-ray.

In our sample, a total of 8 BLAGN were detected, of which 5 have $L_X > 10^{44}$ ergs s^{-1} and therefore are classified, using the threshold of 10^{44} ergs s^{-1} as "quasars" (Hasinger, Miyaji, & Schmidt, 2005); these sources are 1H070m491_s1, 3C279_sA01133, GRB130925A_s1, MCG_01_24_012_sA5 and NGC1313_X1X2_s1. The average redshift for the broad line sample is $< z >_{BL} = 1.33$, which is much higher than the value found for the NL X-ray sources, with mean redshift of $< z >_{NL} = 0.46$. The range of luminosities for the NL sources is also lower than the BL sources, with a mean luminosity for both sources

as $< L >_{NL} = 4.8 \times 10^{43}$ erg s^{-1} and $< L >_{BL} = 5.9 \times 10^{44}$ erg s^{-1}. This is clearly explained by the higher optical brightness of unobscured AGN relative to other X-ray emitters (Treister et al., 2005).

The optical spectral properties of the sources are not relatively diverse; see figure 5.1. The sources clasified as NLAGNs are spread in luminosities between 6.4×10^{42} to 2.1×10^{44} erg s^{-1}. Instead, the BLAGNs sources are in a limited range of luminosities between 1.5×10^{43} to 4.8×10^{45} erg s^{-1}. If the lowest luminosity source is excluded (VelaX1_s1 is a BLAGN with $L_{10-40\ \mathrm{keV}} = 1.92 \times 10^{43}$ erg s^{-1}), it is clear that the BLAGNs are in the highest luminosities with an average of $< L_{10-40\ \mathrm{keV}} >_{BL} \approx 8 \times 10^{44}$ erg s^{-1}.

Thus, in conclusion, Magellan/Gemini-S sources belong to $\approx 10\%$ from the entire sample in the luminosity range $L_{10-40\ \mathrm{keV}} = 10^{44-45}$ erg s^{-1}, which involves, the quasars in the sample.

5.2 Band Ratios

Using the definition from L16, *NuSTAR* hard-to-soft band ratios (BR$_{Nu}$) are calculated as the hard to soft band count rates (equation 5.1). For sources with full band counts of $S_{net} > 100$, and with a detection in at least one of the soft or hard bands, L16 derived an effective photon index (Γ_{eff}); i.e., the spectral slope of a power law spectrum that is required to produce a given band ratio.

$$BR_{Nu} = \frac{8 - 24keV}{3 - 8keV} \tag{5.1}$$

While obscured AGNs can crudely be identified using BR$_{Nu}$ alone, an estimate of the column density requires additional knowledge of the source redshifts, which shift the key spectral features (e.g., the photoelectric absorption cut-off) across the observed energy bands (L16). Here, we use the combination of BR$_{Nu}$ and the source redshifts to identify potential highly obscured objects. Figure 5.2 shows BR$_{Nu}$ versus redshift for the Magellan/Gemini-S sample along with those expected for absorbed power-law emission from an AGN.

To provide direct measurements on the presence of absorption we jointly fitted an absorbed power-law model using the components `zwabs*pow` in `xspec`. As can be seen from Figure 5.2, the shaded regions and the dotted one show the range of expected BR$_{Nu}$ for AGNs with $N_H < 10^{23}$ cm^{-2} and $N_H \sim 5 \times 10^{23}$ cm^{-2}, for an intrinsic spectral slope of

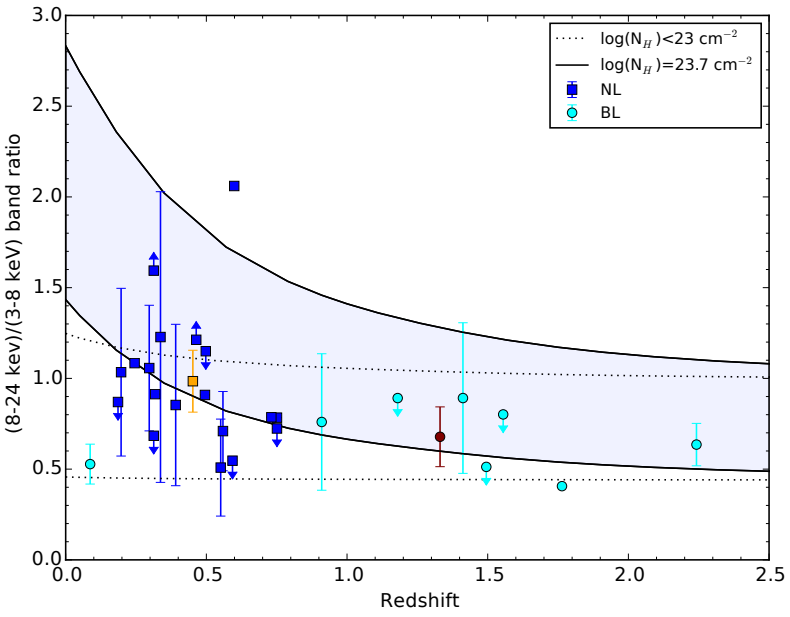

FIGURE 5.2: *NuSTAR* band ratio versus redshifts for this work

$\Gamma = 1.8 \pm 0.5$; the dotted and solid curves indicate the maximum extents in band ratio for $N_{H<}10^{23}$ cm^{-2} and $N_H = 5 \times 10^{23}$ cm^{-2}, respectively.

According L16, given the high X-ray energies probed by *NuSTAR*, the evidence for absorption can be only clearly identified on the basis of the X-ray BR_{Nu} for the most heavily obscured AGNs ($N_H \lesssim 5{\times}10^{23}$ cm^{-2}) at $z \lesssim 0.5$.

As can be seen from Figure 5.2, 27 of the Magellan/Gemini-S sources have been able to calculate X-ray band ratios, 19 of them are NL, and only four NLAGN are consistent with an absorbed $N_H = 5 \times 10^{23}$ cm^{-2}. These four objects are: Super_Antennae_sA5, Fair_All_0272_sA3, NGC3256_s1 and NGC7582_s1.

From Figure 5.2 we identify 12 sources that correspond to the class unobsorbed AGNs which belong to the region of $N_H < 10^{23}$ cm^{-2}. Of the 12 sources, three are BLAGN (3C279 sA01133, MCG_01_24_012_sA5 and PSRJ0437m4715_s5) and the remaining are NLAGN. There are sources with errors that do not allow us to obtain a good constraint on the N_H (NGC1313_s2, NGC1365_s3, PDS456_s2 and PKS1552m331_FIELD_s1).

Figure 5.3 shows the hard to soft band ratios (BR_{Nu}) for the sources from the *NuSTAR* Serendipitous survey studied in this thesis, as a function of full-band (3−24 keV) count rate. In order to examine the results for extragalactic sources only, we removed sources which are spectroscopically confirmed as having $z = 0$. Following L16, we mark the

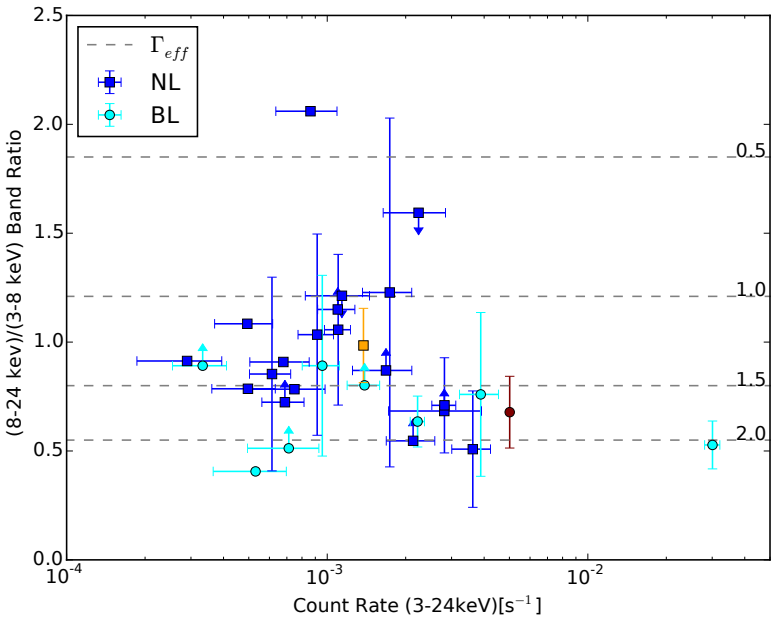

FIGURE 5.3: The *NuSTAR* 8−24 to 3−8 keV band ratio (BR_{Nu}) versus full-band (3−24 keV) count rate for the sources studied in this work.

spectral slopes (Γ_{eff}) corresponding to the band ratios with dotted horizontal lines in Figure 5.3.

We identified 3 out of 4 NLAGNs as candidates with higher level of absorption and being consistent with spectral slope $\Gamma_{eff} > 1$; and those three BLAGNs (mentioned above) were identified as unabsorbed candidates and consistent with $\Gamma_{eff} < 2$. The dependence of the spectral slope to the absorption was expected, because objects with high column densities have to have a flatter spectra to be detectable, meaning they have enough flux in the hard X-ray band to surmount the absorption (Bekmann, 1996).

We computed the average of the band ratio for the two classes and show them in Figures 5.2 and 5.3 (the orange square for NLAGN and the maroon circle for BLAGN). For NLAGNs the band ratio has an average value of 0.98, while for BLAGNs it is 0.68. The higher value of the band ratio observed in the NLAGNs over the other is consistent with the amount of obscuration expected in these sources.

Using a combination of Hardness Ratio (HR) and X-ray luminosity together with optical spectroscopy is very useful for classifying X-ray sources (Szokoly et al., 2004). The HR is defined by the following equation:

$$HR = \frac{H - S}{H + S} \tag{5.2}$$

where S and H are the count rates in the soft and hard bands, respectively. This is illustrated in Figure 5.4 which shows the observed hardness ratios as a function of redshift.

X-ray hardness ratio is an indicator of the intrinsic spectrum which can be used over a wide range of SNR (Wilkes et al., 2013). Assuming the primary power law dominates and that its spectral index is similar in all sources, the hardness ratio statistically indicates the amount of obscuration.

NuSTAR is less sensitive to obscuration, therefore the HR does not contribute to the analysis on the obscuration of the sources, and less to high redshift. One way of demonstrating this effect is by plotting N_H lines in the HR plane as a function of z. Now, redshift and the type of the source are basically equivalent in this study. The average of HR for different z bins are shown in Figure 5.4. It is clear that the difference in the HR for BLAGNs and for NLAGNs depends on redshift, as is expected. It is worth highlighting that for $z < 0.5$ there is a significant difference in the HR value for NL and BLAGNs, due to the above mentioned obscuration effects in X-rays which is much stronger at low redshift. This effect is also seen in the redshift bin, $z = 0.5 - 1$, where the HR is almost the same, and it disappears at $z > 1$.

There is also a clear trend in hardness ratios which decreases with redshift. This effect also was studied by Hasinger (2008), they explained that at higher redshifts the exponential low-energy cutoff in the X-ray spectra of absorbed sources shifts toward lower energies. The latter effect leads to a degeneracy between absorbed and unabsorbed X-ray sources at high redshifts, which can no longer be distinguished using their hardness ratios (Hasinger, 2008).

A similar and expected relation can be inferred from Figure 5.5, which shows the relation between the average HR for different X-ray luminosity bins. In bins, $L_{10-40\ \mathrm{keV}} = 10^{43-44}$ and $L_{10-40\ \mathrm{keV}} = 10^{44-45}$ erg s^{-1}, the HR of NLAGNs is higher than BLAGNs. Moreover, a slight increasing trend in the HR for BLAGNs in luminosity was also inferred.

5.3 The X-ray-optical flux plane

To overcome the difficulties of classification in either the optical or the X-ray bands, a combined optical/X-ray scheme has been introduced (e.g. Szokoly et al., 2004).

The X-ray-to-optical flux ratio (f_X/f_{opt}) is a powerful tool in the visual identification of X-ray sources (Maccacaro et al., 1988). This flux ratio is defined as the ratio between the observed X-ray flux in the $3 - 24$ keV energy band and the optical R band flux, and is due to a combination of nuclear and galaxy emission. X-ray to optical flux ratio suggest

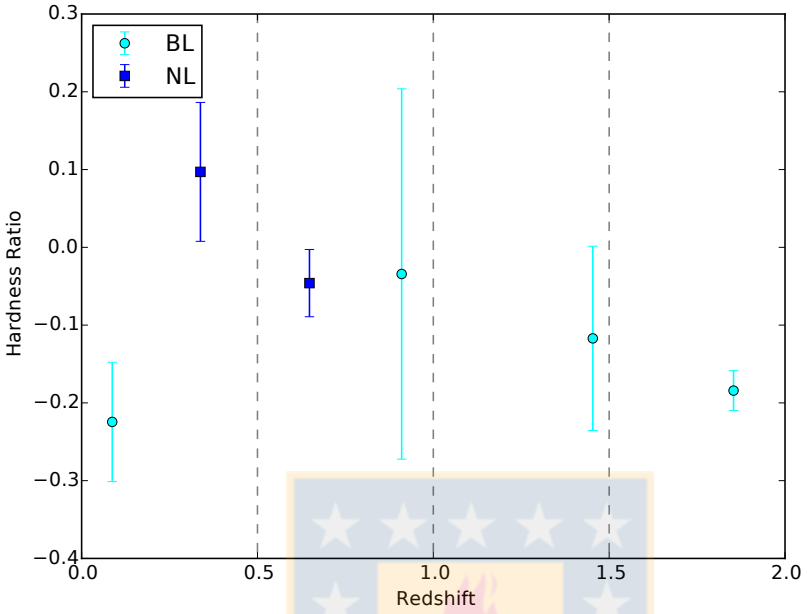

FIGURE 5.4: The hardness ratio (HR) as a function of redshift; own elaboration.

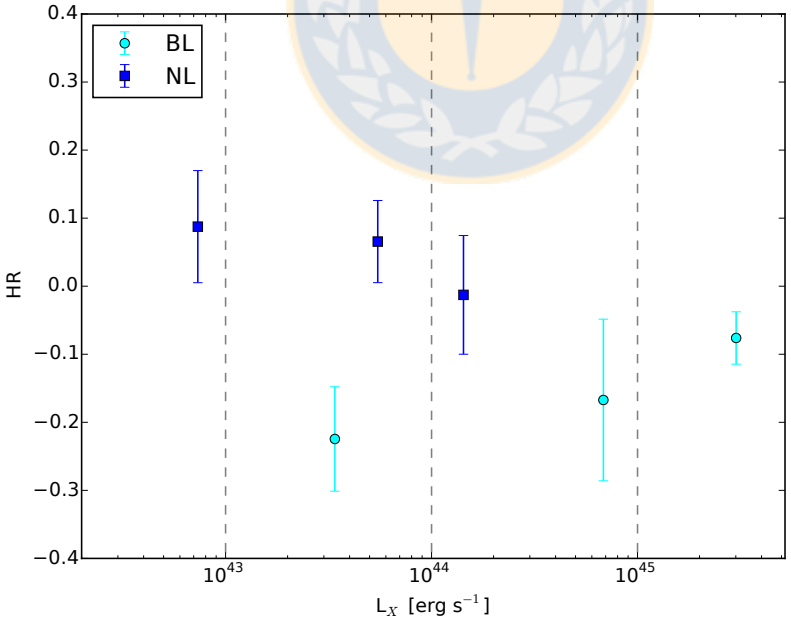

FIGURE 5.5: HR vs. total (10−40 keV) X-ray luminosity; own elaboration.

different class of obscured sources. In type-1 AGN the ratio is mostly due to the nuclear emission in both bands and thus is mainly dependent on the AGN X-ray spectra. As the obscuration of the source increases, the contribution from the galaxy light becomes more important in the optical band, and the $f_X/f_{\rm opt}$ ratio becomes roughly a ratio between the nuclear X-ray emission and the optical host galaxy emission. For highly luminous obscured AGN the highest effect of the $f_X/f_{\rm opt}$ ratio can be produced as the result of the R band luminosity's minimal scatter around the mean value ($L_R = 10^{11} L_\odot$), while the luminosity spans a wider range (Fiore et al., 2003; Comastri & Fiore, 2004).

The normal galaxies have typically $f_X/f_{\rm opt} \lesssim 0.1$, while the dominant X-ray selected AGN population has $0.1 < f_X/f_{opt} < 10$, with the obscured AGN having on average $f_X/f_{\rm opt} \gtrsim 10$ (Maccacaro et al., 1988). Thus, a high X-ray-to-optical flux ratio ($f_X/f_{\rm opt} \gtrsim 10$, at least ten times higher than that typical for X-ray selected AGN) is considered to be a good tracer of highly obscured high redshift AGN (type-2 QSO; e.g. Fiore et al., 2003).

In order to investigate a possible relation between X-ray and optical emission for different source classes, we investigate the plane using the optical R band for the Magellan/Gemini-S *NuSTAR* Serendipitous sources, which provides a relatively large hard X-ray selected sample spanning comparatively a wide flux range. We show in Figure 5.6 that a large fraction of the sources spans the typical X-ray-to-optical flux ratio of AGN.

In the hard band (Figure 5.6), where the effect of the absorption is weaker, the range of fluxes covered by the NLAGN is the same as that of the BLAGN sample. We also note that the large majority of the sources (92.3%) are confined to a region with -1 $< log(f_X/f_{\rm opt}) < 1$, typical values for AGNs. The higher values of $log(f_X/f_{\rm opt})$ generally indicate more obscuration. According to the Figure 5.6, only 4 of the serendipitous have a high X-ray-to-optical ($log(f_X/f_{\rm opt}) > 1$) flux ratio, and none of them were studied in this thesis.

The low X-ray-to-optical flux ratio regime ($log(f_X/f_{\rm opt}) < -1$) means that the sources has lower emission in X-rays than the typical AGNs. Indeed, the are only two sources that were identified with $log(f_X/f_{\rm opt}) < -1$ are PDS456_s2 and NGC4945_sA01142. This may be due to several reasons. The first one is that these sources are not an AGNs, but are normal galaxies where their emission comes from HMXB ($L_X < 10^{39}$ erg s^{-1} Grimm et al., 2002). The second reason is that maybe these sources are thought to be populated by low-luminosity AGNs (LLAGNs, $L_X < 10^{42}$ erg s^{-1}) and "normal" galaxies (Hornschemeier et al., 2003). This is not the case because these two serendipitous have luminosities of 8.92×10^{42} erg s^{-1} and 1.3×10^{44} erg s^{-1} respectively. The most reasonable case is that these AGNs are highly obscured, so that the emission in X-rays is suppressed

and the emission in the optical is dominated by the galaxy. This is well supported because we only detect NL in both of the sources.

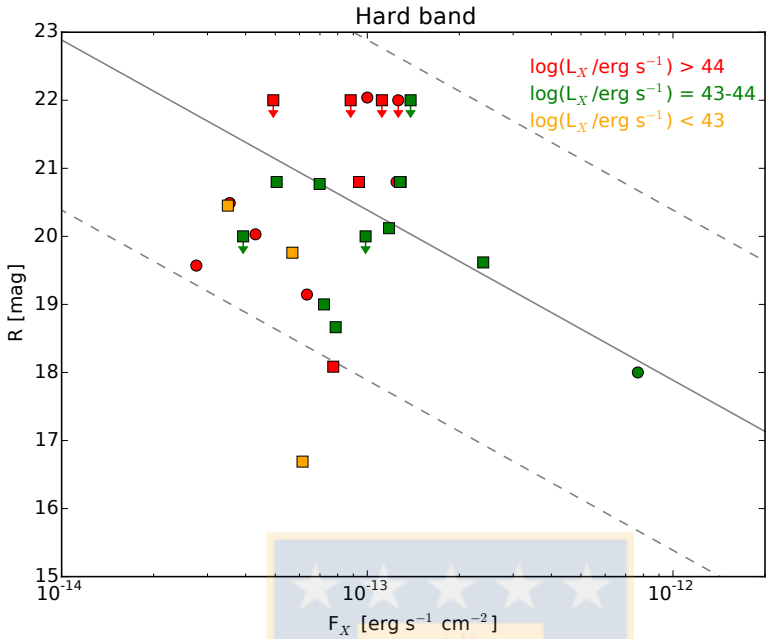

FIGURE 5.6: *R*-band optical magnitude versus X-ray flux in hard X-ray (8−24 keV) from this work.

The Figures 5.7 and 5.8 shows that PDS456_s2 and NGC4945_sA01142 are in the $log(f_X/f_{\rm opt}) < -1$ zone with fluxes in the hard band of $f_{8-24{\rm keV}} \approx 10^{-13.5}$ erg cm^{-2} s^{-1} and $f_{8-24{\rm keV}} \approx 10^{-13.1}$ erg cm^{-2} s^{-1}, respectively. The rest of the Magellan/Gemini-S sample are in the region of typical values for AGN. This is not surprising, since in general, the *NuSTAR* Serendipitous sources are confined in this region (-1 < $log(f_X/f_{\rm opt})$ < 1).

If we compared them with the Fiore et al. (2003) sample, we see a clear difference between the type of sources that dominates in this specific region. In this work, the Magellan/Gemini-S sources that dominate the region with $-1 < log(f_X/f_{\rm opt}) < 1$ are NLAGNs, meanwhile in Fiore et al. (2003) BLAGNs dominates the same region. This difference in the dominant population is due to he use data from *Chandra* and *XMM-Newton*, thus his sample includes low luminosities AGNs. hence his sources are two orders of magnitude more sensitive than the *NuSTAR* sources.

A correlation between $f_X/f_{\rm opt}$ and L_X in NLAGN was obtained (Figure 5.9). The blue diagonal line in Figure 5.9 represents the best linear regression between $f_X/f_{\rm opt}$ and $log(L_X)$ for NLAGN. In Figure 5.10, the rest of the *NuSTAR* Serendipitous sources are included, and shows the same correlation.

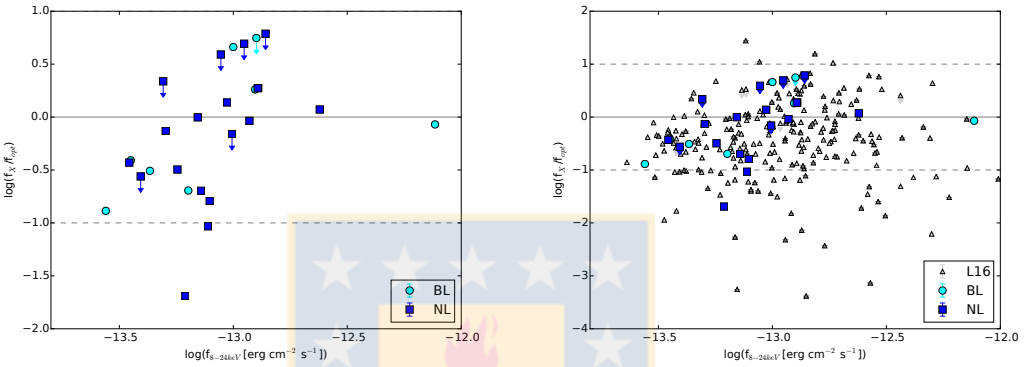

FIGURE 5.7: $f_X/f_{\rm opt}$ versus X-ray flux in hard X-ray (8-24keV) from this work.

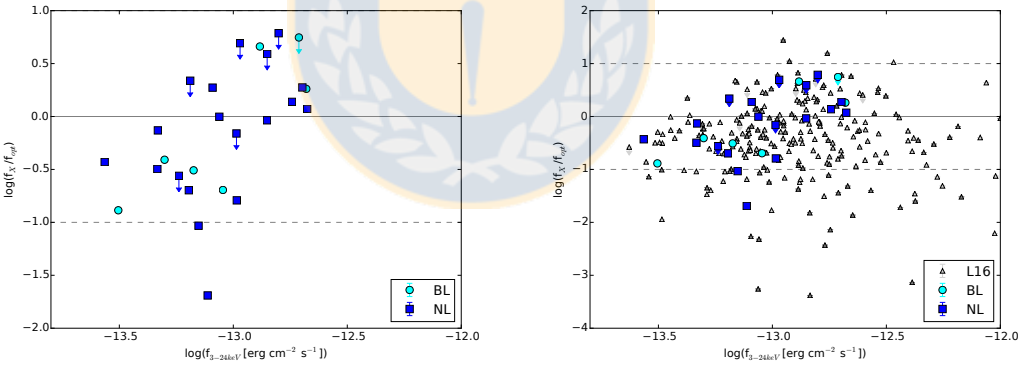

FIGURE 5.8: $f_X/f_{\rm opt}$ versus X-ray flux in full X-ray (3-24keV) from this work.

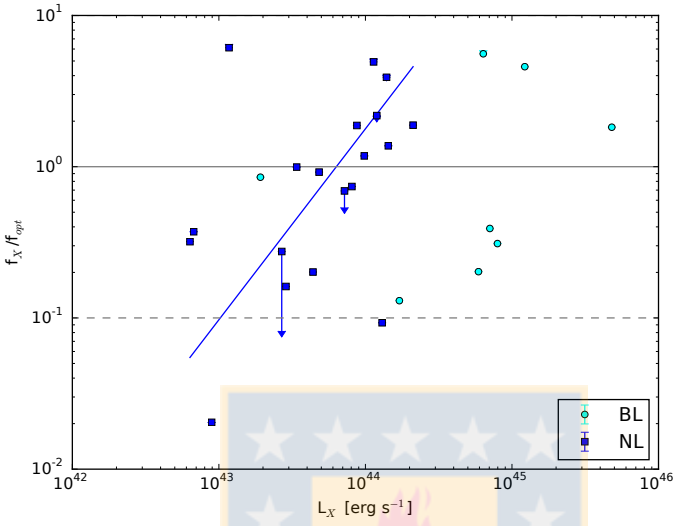

FIGURE 5.9: f_X/f_{opt} versus $L_{10-40\mathrm{keV}}$ from this work.

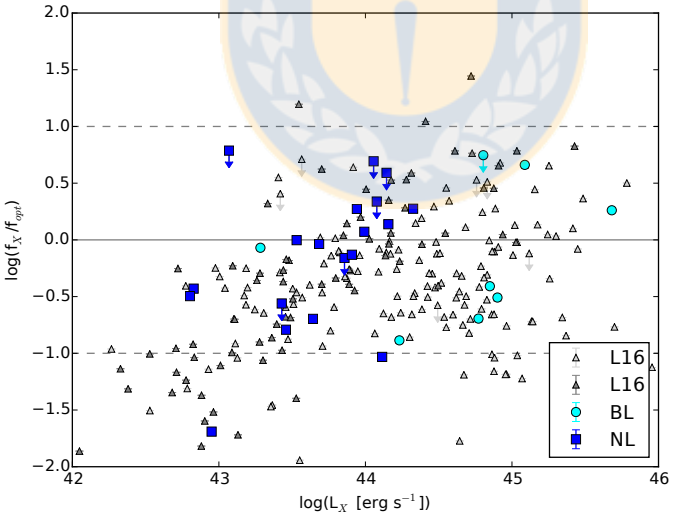

FIGURE 5.10: f_X/f_{opt} versus $L_{10-40\mathrm{keV}}$ in logarithmic scale for the whole Serendipitous from this work.

Chapter 6

Conclusions

In this thesis, the optical and the X-ray analysis has been presented for a subsample from the *NuSTAR* Serendipitous survey, selected according to their possible detection using the Magellan and Gemini-S telescopes and their magnitudes ($R > 20$). We were able to observed 43 sources, but in 39 of them we detected continuum. Thereby, we were able to measure redshifts and classify 35 sources, according to their emission lines. This is critical in the analysis of intrinsic source properties such as luminosity and the amount of obscuration (L16). We use the following spectrographs in this thesis, MagE, IMACS and GMOS. They have typical observed-frame wavelength range covered of $\lambda \sim 3500 - 9000$ Å.

While 35 sources account for only 13% of the overall spectroscopically identified sample from the *NuSTAR* Serendipitous survey, they form a larger percentage (20/90) of the optically faint sample from the same catalog.

As the sources belong to the *NuSTAR* observations, it is expected that most of the sources will be AGN, however, a small amount turned out to be galactic sources. The optical spectroscopic data described in Chapter 2 allows us to group the sources into 3 classes based on their spectral features:

- 5 galactic stars: they show Balmer emission lines. These features show us that these 5 sources are HXMB-Be stars, and indicates the presence of a circumstellar disk.
- 8 sources as Broad-Lined AGN (BLAGN): if they have broad emission lines, such as CIII] λ1909Å, Mg II λ2800Å. These sources include quasars, which in the unified theory are objects viewed with the obscuring torus face on and the central nuclear region unobscured.

- 22 sources as Narrow-Lined AGN (NLAGN): these sources with high-ionization emission lines are classified as NLAGN. Typical high-ionization lines indicating the presence of an AGN are [OIII] λ5007,4959Å, and [NII] λ6583Å in combination with low-ionization lines such as H_β, H_α, etc. These sources are the obscured AGN in the unified model viewed edge-on with an obscured view of the nucleus.

This optical classification is independent of the sources' X-ray properties.

The redshifts for the extragalactic sources cover a large range, from z = 0.0867 to 2.242. For these objects with independent detection in the high-energy band ($8-24$ keV), to which *NuSTAR* is uniquely sensitive, the median redshift is $< z > = 0.612$. We also highlight that most of the high redshift sources are BLAGN, with a redshift up to 2.242. These ones also have fainter optical counterparts with optical magnitudes in the $19-22$ range. For the lower redshift region we see that the NLAGN is the dominant class in a range of magnitude between $18-22$ mag with a median redshift up to 0.75.

We also analyzed the X-rays luminosities for the Magellan/Gemini-S sources. Of the 30 extragalactic sources detected, the NLAGN are less luminous in comparison to the BLAGN. Moreover, 7 out of 8 of these ones are in the threshold that defines "X-ray quasars" ($L_X > 10^{44}$ erg s^{-1} section 5.1). This is due to BL sources being less affected by obscuration.

Considering the results obtained from the X-ray spectral analysis and the BR definition in combination with the models for N_H, it can be concluded that the NL sources have higher values, since four sources have values consistent with being obscured at $N_H > 5 \times 10^{23}$ cm^{-2}. Considering the results from f_X/f_{opt} plane for the extragalactic sources it can be concluded that the 20% of the fainter sources from the *NuSTAR* Serendipitous survey have typical AGN values of $-1 < log(f_X/f_{opt}) < 1$. However, two of these sources have values, $log(f_X/f_{opt}) < -1$; we finally considered that these sources could declare them as highly obscured NLAGNs.

According to the definition of HR (eq. 5.2), we studied the difference of the values for NLAGN and BLAGN as an approximation for the study of obscuration. The difference is related to the redshift and luminosities, such that at lower z, NL sources tend to have higher HR values. Thus, at lower redshift ($z < 0.5$) there is a large difference in HR between NLAGN and BLAGN. This difference disappears at high redshift ($z > 0.5$), however the HR value changes as a function of redshift. A similar result was also obtained for the case of luminosity.

Finally, we concluded the population of the 13% of the *NuSTAR* Serendipitous that were analyzed in this thesis is dominated by sources identified as NLAGNs. This is

exactly the opposite if we considered the total Serendipitous sample, where the majority is dominated by sources classified as BLAGN. However, this sample of 30 extragalactic sources are not enough for a complete statistic on the population that resides in the CXB peak obtained by *NuSTAR*, only for the fainter ($R > 20$ mag) ones.

Bibliography

Aird, J., Alexander, D. M., Ballantyne, D. R., et al. 2015, ApJ, 815, 66

Ajello M., et al., 2008, ApJ, 673, 96-113

Alexander D. M., et al., 2013, ApJ, 773, 125

Antonucci R., 1993, ARA&A, 31, 473

Ballantyne D. R., Draper A. R., Madsen K. K., Rigby J. R., Treister E., 2011, ApJ, 736, 56

Barger, A. J., Cowie, L. L., Capak, P., et al. 2003, AJ, 126, 632

Beckmann, 1996, thesis, Hamburg University, "X-ray spectral slope of AGN in the ROSAT All Sky Survey"

Bigelow B. C., Dressler A. M., Shectman S. A., Epps H. W., 1998, SPIE, 3355, 225

Brandt W. N., Hasinger G., 2005, ARA&A, 43, 827

Burlon D., Ajello M., Greiner J., Comastri A., Merloni A., Gehrels N., 2011, ApJ, 728, 58

Churazov, E., Sunyaev, R., Revnivtsev, M., et al. 2007, A&A, 467, 529

Civano F., et al., 2015, ApJ, 808, 185

Comastri A., Fiore F., 2004, Ap&SS, 294, 63

Croton D. J., et al., 2006, MNRAS, 365, 11

Curtis, H. D. 1918, Publications of Lick Observatory, 13, 9

Davies R. L., et al., 1997, SPIE, 2871, 1099

De Luca, A., & Molendi, S. 2004, A&A, 419, 837

Eckart, M. E., Stern, D., Helfand, D. J., et al. 2006, ApJS, 165, 19

Elvis M., Maccacaro T., Wilson A. S., Ward M. J., Penston M. V., Fosbury R. A. E., Perola G. C., 1978, MNRAS, 183, 129

Valentino Esposito, Active Galactic Nuclei at High Energies Spectral Properties and The Cosmic X-ray Background, thesis doctoral, Univ Geneve 2016, no. Sc. 4945.

Fabian A. C., Barcons X., 1992, ARA&A, 30, 429

Fiore F., et al., 2003, A&A, 409, 79

Georgantopoulos I., Stewart G. C., Shanks T., Boyle B. J., Griffiths R. E., 1996, MNRAS, 280, 276

Giacconi R., Gursky H., Paolini F. R., Rossi B. B., 1962, PhRvL, 9, 439

Giacconi R., et al., 2002, ApJS, 139, 369

Gilli R., 2004, AdSpR, 34, 2470

Grimm, H.-J., Gilfanov, M., & Sunyaev, R. 2002, A&A, 391, 923

Gruber, D. E., Matteson, J. L., Peterson, L. E., & Jung, G. V. 1999, ApJ, 520, 124

Gehrels, N. 1986, ApJ, 303, 336

Harrison F. A., et al., 2016, ApJ, 831, 185

Harrison F. A., et al., 2013, ApJ, 770, 103

Hasinger G., 2008, A&A, 490, 905

Hasinger G., et al., 2001, A&A, 365, L45

Hasinger G., Miyaji T., Schmidt M., 2005, A&A, 441, 417

Hickox R. C., Markevitch M., 2006, ApJ, 645, 95

Hornschemeier A. E., Bauer F. E., Alexander D. M., Brandt W. N., Sargent W. L. W., Vignali C., Garmire G. P., Schneider D. P., 2003, AN, 324, 12

Kelson D. D., 2003, PASP, 115, 688

Kraft R. P., Burrows D. N., Nousek J. A., 1991, ApJ, 374, 344

Krivonos R., Revnivtsev M., Lutovinov A., Sazonov S., Churazov E., Sunyaev R., 2007, A&A, 475, 775

Lansbury G. B., et al., 2016, arXiv, arXiv:1612.06389

Lehmann I., et al., 2001, AIPC, 599, 189

Maccacaro T., Gioia I. M., Wolter A., Zamorani G., Stocke J. T., 1988, ApJ, 326, 680

Marshall J. L., et al., 2008, SPIE, 7014, 701454

Martin, D. C., Fanson, J., Schiminovich, D., et al. 2005, ApJL, 619, L1

Mullaney J. R., et al., 2015, ApJ, 808, 184

Reig P., 2004, ESASP, 552, 373

Setti G., Woltjer L., 1989, A&A, 224, L21

Skrutskie, M. F., Cutri, R. M., Stiening, R., et al. 2006, AJ, 131, 1163

Szokoly G. P., et al., 2004, ApJS, 155, 271

Treister E., Urry C. M., Virani S., 2009, ApJ, 696, 110

Treister, E., Castander, F. J., Maccarone, T. J., et al. 2005, ApJ, 621, 104

Treister E., Urry C. M., Van Duyne J., GOODS AGN Team, 2005, MmSAI, 76, 142

Treister E., Urry C. M., 2005, ApJ, 630, 115

Treister, E., Urry, C. M., Chatzichristou, E., et al. 2004, ApJ, 616, 123

Tueller J., Mushotzky R. F., Barthelmy S., Cannizzo J. K., Gehrels N., Markwardt C. B., Skinner G. K., Winter L. M., 2008, ApJ, 681, 113-127

Ueda Y., Akiyama M., Ohta K., Miyaji T., 2003, ApJ, 598, 886

Urry C. M., Padovani P., 1995, PASP, 107, 803

Urry C. M., Treister E., 2007, arXiv, arXiv:0712.1041

Veilleux S., Osterbrock D. E., 1987, NASCP, 2466,

Wilkes B. J., et al., 2013, ApJ, 773, 15

Wright, E. L., Eisenhardt, P. R. M., Mainzer, A. K., et al. 2010, AJ, 140, 1868-1881